WIND NOISE PREDICTION OF A CAR MODEL THROUGH SOLUTIONS OF NAVIER-STOKES AND FFOWCS WILLIAMS & HAWKINGS EQUATIONS

A THESIS SUBMITTED TO
THE GRADUATE SCHOOL OF NATURAL AND APPLIED SCIENCES
OF
MIDDLE EAST TECHNICAL UNIVERSITY

BY

BARAN GÜMÜŞ

IN PARTIAL FULFILLMENT OF THE REQUIREMENTS
FOR
THE DEGREE OF MASTER OF SCIENCE
IN
AEROSPACE ENGINEERING

JUNE 2017

Approval of the thesis:

WIND NOISE PREDICTION OF A CAR MODEL THROUGH SOLUTIONS OF NAVIER-STOKES AND FFOWCS WILLIAMS & HAWKINGS EQUATIONS

submitted by **BARAN GÜMÜŞ** in partial fulfillment of the requirements for the degree of **Master of Science in Aerospace Engineering Department, Middle East Technical University** by,

Prof. Dr. Gülbin Dural Ünver
Dean, Graduate School of **Natural and Applied Sciences**

Prof. Dr. Ozan Tekinalp
Head of Department, **Aerospace Engineering**

Prof. Dr. Yusuf Özyörük
Supervisor, **Aerospace Engineering Dept., METU**

Examining Committee Members

Prof. Dr. İsmail Hakkı Tuncer
Aerospace Engineering Department, METU

Prof. Dr. Yusuf Özyörük
Aerospace Engineering Department, METU

Assoc. Prof. Dr. Sinan Eyi
Aerospace Engineering Department, METU

Prof. Dr. Mehmet Çalışkan
Mechanical Engineering Department, METU

Asst. Dr. Polat Şendur
Mechanical Engineering Department, Ozyegin University

Date: 14.06.2017

I hereby declare that all information in this document has been obtained and presented in accordance with academic rules and ethical conduct. I also declare that, as required by these rules and conduct, I have fully cited and referenced all material and results that are not original to this work.

Name, Last name : BARAN GÜMÜŞ

Signature :

ABSTRACT

WIND NOISE PREDICTION OF A CAR MODEL THROUGH SOLUTIONS OF NAVIER-STOKES AND FFOWCS WILLIAMS & HAWKINGS EQUATIONS

Gümüş, Baran
M.S., Department of Aerospace Engineering
Supervisor: Prof. Dr. Yusuf Özyörük

June 2017, 74 pages

Vehicles are getting quieter by virtue of recent technological improvements, but still wind noise of vehicles is one of the major contributors of total vehicle noise. It must be limited to design quieter vehicles. Compared to aeroacoustic wind tunnel tests, successful aeroacoustic predictions are cheaper and more practical. Thus, accurate flow simulation and computational aeroacoustics (CAA) methods to predict vehicle aerodynamic noise are investigated and discussed in this thesis. Moreover, accurate flow simulations are needed for successful aeroacoustic predictions and therefore higher order solution, mesh size limitation, appropriate boundary layer modelling and suitable turbulence modelling are required. Required flow simulation is performed by commercial FLUENT software. Subsequently, Ffowcs Williams & Hawkings (FW-H) method is used for far field wind noise calculation due to its robust and fast nature. Hence, aeroacoustic prediction is performed by a FORTRAN code for FW-H solution of far field wind noise. Results are compared to wind tunnel tests for verification.

Keywords: wind noise, computational aeroacoustics, aeroacoustic wind tunnel test, DDES, FW-H

ÖZ

BİR ARABA MODELİNİN RÜZGAR GÜRÜLTÜSÜNÜN NAVIER-STOKES VE FFOWCS WILLIAMS & HAWKINGS DENKLEMLERİNİN ÇÖZÜMLERİ İLE TAHMİNİ

Gümüş, Baran
Yüksek Lisans, Havacılık ve Uzay Mühendisliği Bölümü
Tez Yöneticisi: Prof. Dr. Yusuf Özyörük

Haziran 2017, 74 sayfa

Taşıtlar güncel teknolojik gelişmeler sayesinde daha sessiz hale gelmektedir, yine de toplam taşıt gürültüsüne en çok katkı sağlayan faktörlerden biri rüzgar gürültüsüdür. Daha sessiz taşıtlar dizayn edebilmek için rüzgar gürültüsü sınırlandırılmalıdır. Hesaplamalı aeroakustik yöntemler, rüzgar tüneli testlerine kıyasla daha ucuz ve pratiktir. Dolayısıyla, bu tezde isabetli akış hesaplaması ve hesaplamalı aeroakustik (CAA) metotları araştırılmıştır ve ele alınmıştır. Başarılı bir rüzgar gürültüsü tahmini için başarılı bir akış çözümü gereklidir. Dolayısıyla, yüksek dereceli çözümler, sınırlı eleman boyutu limiti, uygun sınır tabaka ve türbülans modellemeleri gerekmektedir. Bunlar için gerekli akış çözümü FLUENT yazılımı ile gerçekleştirilmiştir. Ardından, uzak noktadaki rüzgar gürültüsü hesaplaması için, yapısındaki dayanıklılık ve hızlılık sebebiyle Ffowcs Williams & Hawkings (FW-H) metodu kullanılmıştır. Sonunda, uzak alandaki gürültüyü FW-H metodu hesaplamak için bir FORTRAN kodu kullanılmıştır. Doğrulamak amacıyla sonuçlar rüzgar tüneli testleri ile kıyaslanmıştır.

Anahtar Kelimeler: rüzgar gürültüsü, hesaplamalı aeroakustik, aeroakustik rüzgar tüneli testi, DDES, FW-H

To people who are in pursuit of new horizons

ACKNOWLEDGMENTS

First of all, I would like to express my gratitudes to my thesis supervisor Prof. Dr. Yusuf Özyörük for his time, advice, support and encouragements throughout the thesis. I also wish to thank Prof. Özyörük for accepting to supervise me, considering that I do not reside in Ankara.

I would like to thank to my friend, research assistant Özgür Yalçın for his guidance and experience on a similar subject.

I wish to present my gratitude to Çağrı Kırseven and Özgür Yalçın for their support on academic procedures and making it easier for me to continue my post graduate studies, even I reside in İstanbul.

I would also like to thank Ford Otosan for given opportunity to do this research and allowing to use necessary resources.

I would like to thank my colleagues Ezgi Güneş, Umut Özcan, Can Koman and my former supervisor Dr. Polat Şendur for their contributions and supports.

I wish to express my gratitude to my dear mother, father, brother and whole my family for their support during my whole education life and for sharing happiness in good times, even in stressful times.

I would like to thank to my beloved wife Fatma for making the world more green and better place for me, for her support, for her joyful heart and for shared happiness; considering the stressful, pressurized times and travels.

I would like to thank my adorable cat Zıpır for her calming, relaxing and funny behavior.

Finally, I wish to express my thanks to radio programmers Cenk Durmazel, Erdem Uygan and Modern Sabahlar team; Fahir Öğünç, Oktay Demirci and Ege Kayacan for their radio programs that makes me settle and smile during the stressful times during my post graduate education.

TABLE OF CONTENTS

CHAPTERS

LIST OF TABLES

TABLES

LIST OF FIGURES

FIGURES

LIST OF ABBREVIATIONS

CAA	Computational Aeroacoustics
CFD	Computational Fluid Dynamics
CFL	Courant-Friedrichs-Lewy
CS	Control Surface
CV	Control Volume
DDES	Delayed Detached Eddy Simulation
DES	Detached Eddy Simulation
DNS	Direct Numerical Simulation
FFT	Fast Fourier Transform
FW-H	Ffowcs Williams-Hawkings
HPC	High Performance Computing
LCV	Light Commercial Vehicle
LEE	Linearized Euler Equations
LES	Large Eddy Simulation
MUSCL	Monotone Upstream-Centered Schemes for Conservation Law
NASA	National Aeronautics and Space Administration
NS	Navier-Stokes
PBN	Pass-by Noise
RANS	Reynolds-Averaged Navier-Stokes
RMS	Root Mean Square
SGS	Subgrid-Scale
$(\ )_i$	Suffix notation
$\overline{(\ )}$	Average of Variables in Time Domain
$(\ )'$	Fluctuations

α	A Quantity on Cell Face
β	Buoyancy
β^*	Prandtl-Glauert Factor
Δt	Time Step
Δx	Largest Grid Spacing in Cartesian Coordinates
δ	Dirac Delta Function
δ_{ij}	Kronecker Delta
ϵ	Turbulent Dissipation
ϵ_{ijk}	Levi-Civita Symbol
η	Closure Coefficient of Realizable $k-\epsilon$ Model
κ	von Karman constant
λ	Wavelength
μ	Dynamic Viscosity
μ_T	Eddy Viscosity
ν	Turbulent Kinematic Viscosity
ν_t	Molecular Kinematic Viscosity
v_i	Velocity Components on FW-H Surface
ξ_i	Axes of Curvilinear Coordinates
ρ	Density
σ_{ij}	Stress Tensor
$\sigma_k, \sigma_\epsilon$	Closure Coefficients for Rate of Dissipation Equation
τ_{ij}	Reynolds Stress Tensor
ϕ	Potential Function of a 3D-Monopole Source
φ	Model Constant of Realizable $k-\epsilon$ Model
Ψ	Dummy Constant for Spatial Discretization
Ω	Vorticity
$\widetilde{\Omega_{ij}}$	Rate of Rotation Tensor

$\overline{\Omega_{ij}}$	Mean Rate of Rotation Tensor
ω	Angular Frequency
∇	Gradient Operator
A	Wetted Area
A_0, A_s	Model Constants of Realizable $k-\epsilon$ Model
$\vec{A}$	Area Vector of a Cell Face
c_0	Speed of Sound
$C_{\epsilon 1}, C_{\epsilon 2}, C_{\mu}$	Closure Coefficients for Rate of Dissipation Equation
$C_{3\epsilon}$	Buoyancy Effect on Turbulent Dissipation
C_1, C_2	Closure Coefficients of Realizable $k-\epsilon$ Model
C_d	Drag Coefficient
C_{des}	Isotropic Turbulence Decay Calibration
C_p	Pressure Coefficient
C_s	Smagorinsky Constant
$\tilde{d}$	Length Scale of DES
dB	Decibels
F_d	Length Scale Limiter Term
F_{drag}	Drag Force
F_i	Dipole Source Term
f	Frequency
G	Green’s Function
G_b	Generation of Turbulent Kinetic Energy due to Buoyancy
G_k	Generation of Turbulent Kinetic Energy due to Velocity Gradient
g	Gravity Vector
H	Heaviside Function
I_Q, I_L, I_T	Quadrupole, Dipole, Monopole Terms

i	Complex Number
k	Turbulent Kinetic Energy
L	Characteristic Length
L_s	Mixing Length for Subgrid-Scale
M	Mach Number
N_f	Total Number of Faces of a Cell
$\tilde{n}$	Cell Surface Normal Vector
Pa	Pascals
Pr_t	Turbulent Prandtl Number
p	Pressure
Q	Monopole Source Term
Q_c	Q-Criterion
$\vec{r}$	Distance Between a Cell Centroid to Its Surface
$\tilde{S}$	Model Constant of Realizable $k-\epsilon$ Model
S_{ij}	Mean Strain-Rate Tensor
S_k , S_ϵ	Variable Source Terms
St	Strouhal Number
T	Temperature
T_{ij}	Quadrupole Source Term
t	Time
U_i	Freestream Flow Velocity
u_i	Velocity Components; u, v, w
V	Cell Volume
W	Model Constant of Realizable $k-\epsilon$ Model
x_i	Coordinates; x, y, z
Y_M	Contribution of Compressibility on Turbulence

CHAPTER 1

INTRODUCTION

1.1. Recent Status of Vehicle Noise

Noise pollution is a frequently discussed subject that is limited by regulations. Aircraft and automotive noise are two major contributors of environmental noise pollution [1]. In addition to the regulations, recent technological progress shapes the future of modern vehicles to become quieter. Aircraft, cars and high-speed train development processes include noise oriented design guidelines. Although exterior noise levels are generally limited by regulations, interior noise levels are more passenger focused [2].

Passenger focused noise design is defined in the subject of sound quality. Since it is a highly concentrated aspect in engineering since 1980s, vehicles are getting quieter over time. Figure 1 represents root mean square (RMS) of interior noise levels of 389 automobiles in decibels (dB), with respect to model years from 2008 to 2016 [3]. Statistics of only petrol engines with sizes between 1.2 liters - 1.6 liters are included in the plot. All cars are in A (mini) – B (small) – C (medium) – D (large) segments according to European Commission [4]. All dots in this figure represents interior noise of individual cars, whereas continuous lines stand for mean interior noise of corresponding cars. Interior noise reduction is observable with passing years. The trend between 2008 and 2016 shows that RMS values of interior noise levels for 80 km/h and 140 km/h cruise conditions are reduced by 2.5 dB and 1 dB, respectively.

Contrary to the reduced noise throughout these years, sensitiveness for acoustical comfort also increases with time [5]. On the other hand, there is a conflict between good sound quality and other requirements of attributes. For example, required time to develop a new design is getting tighter, costs are kept low and total weight of vehicle is strictly controlled. These targets must be satisfied with good sound quality.

Interior noise level of a vehicle is generally desired to be low due to its luxurious and comfortable feeling. In order to achieve this task; measurement, analysis and prediction of vehicle noise become important. Therefore, sources of noise should be defined well. Then, necessary actions at early design phases would accomplish the task.

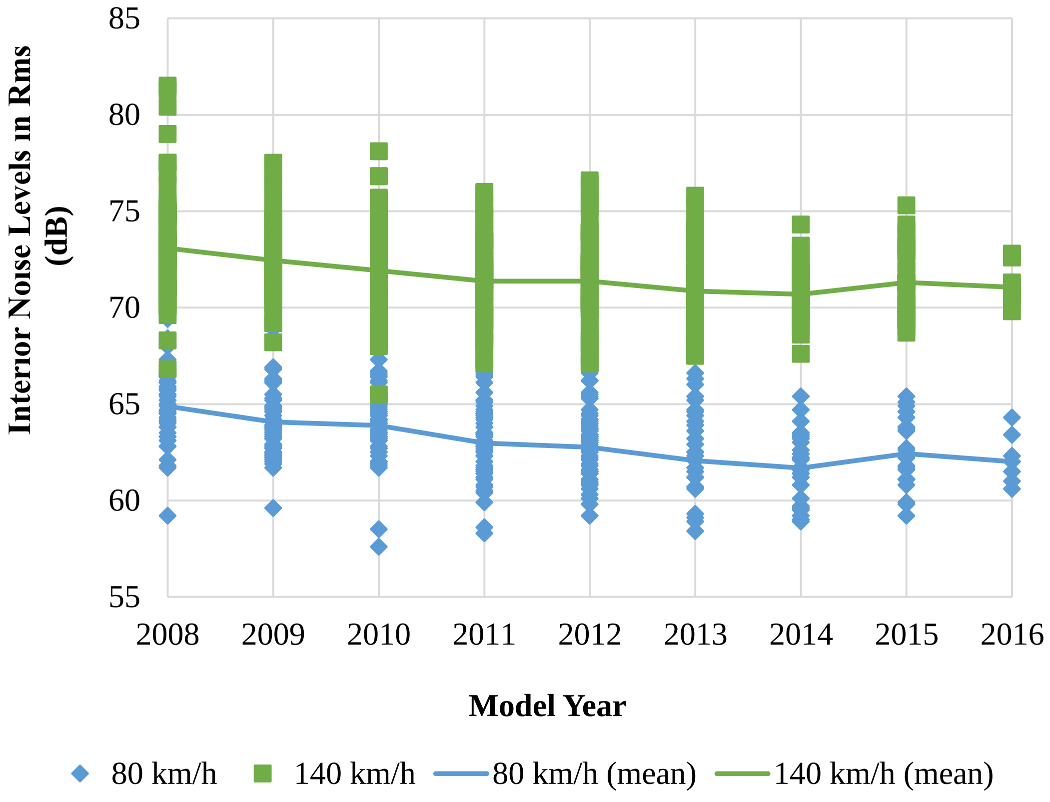

Figure 1: Automobile interior noise levels at 80 km/h and 140 km/h

1.2. Noise Sources on a Vehicle

A noise transfer mechanism consists of three main elements; source, path and receiver as depicted in Figure 2.

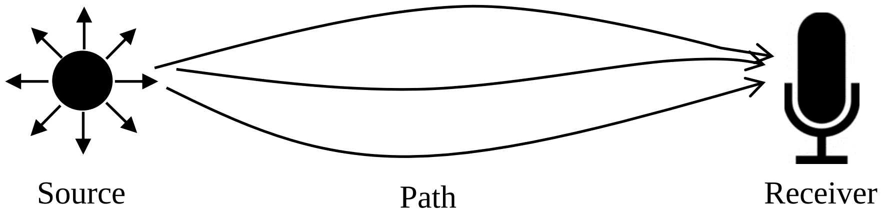

Figure 2: Noise transfer mechanism

Sources of noise can be classified into airborne or structure-borne [6]. Airborne noise is defined as transmission of noise, through consecutive motion of air particles between source and receptor. Similarly, structure-borne noise is transferred from source to receptor via vibrations through solid structure. It can be deduced from Figure 3 that for automotive, structure-borne noise is effective in low and mid frequency range, while airborne noise is dominant at high frequencies [7]. Engine is another powerful noise source, whose effect is transmitted via air and structure. Road and tire contact is also an important noise source for ground vehicles at low and mid frequency range. Wind noise that is created by flow around the vehicle is airborne noise.

Engine contributes in a wide spectrum to noise levels of all types of vehicles. Engine noise reduction on source is a difficult task. However, innovative changes on engine allow significant noise reduction. Hybrid and electric powered cars and high-speed trains encounter noise reduction to a scale that let discussions to “faking” engine noise for safety concerns.

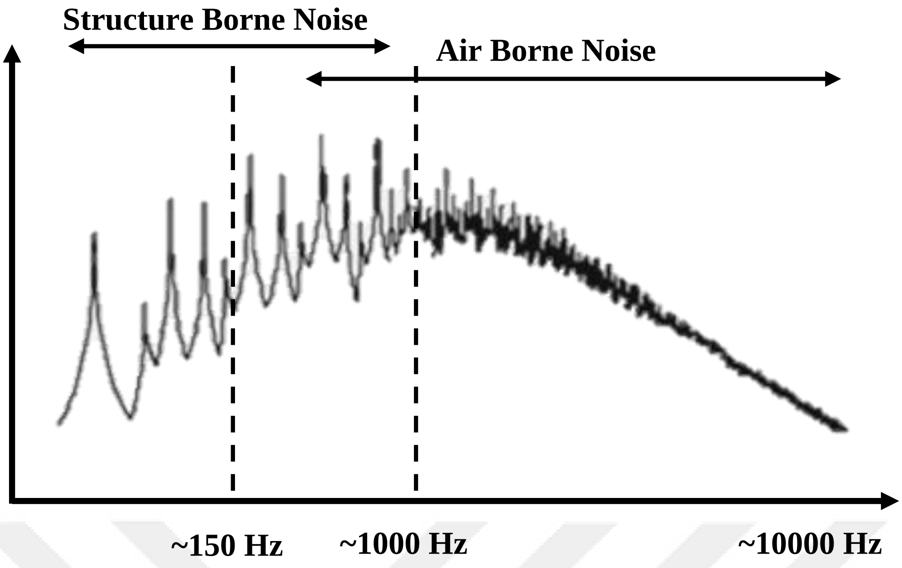

Figure 3: Automotive noise spectrum

Road noise reduction for ground vehicles is possible but costly. It highly depends on tire technology and asphalt grade. The latter depends on geography and weather condition.

Wind noise is defined as pressure fluctuation about medium’s mean pressure [8]. It is also referred as aerodynamic noise, frame noise, shape noise, and airframe noise.

Due to strict regulations and stealth feature, aerodynamic noise has been an important aspect of aviation. Similarly, aeroacoustics development of automobiles and high-speed trains is a topic that draws attention. Pass-by-noise (PBN) regulations exist for automotive and railways. PBN regulations of automotive are at very low speeds, that is, 50 km/h [9]. The regulation is mostly exhaust noise oriented. Whereas, wind noise of a vehicle dominate speeds over 100 km/h, which is quite low compared to aviation speeds, but still important in terms of aerodynamic noise [10]. Because wind noise is proportional to sixth power of velocity [11], it is effective in cruising conditions at higher speeds. Other noise sources do not depend on vehicle speed at this level.

Wind noise prediction by computational techniques exists at system level (landing gear, weapon bay noise, etc.) and vehicle level (full geometry of aircraft) in aviation.

However, wind noise is obtained, most frequently, by tests in automotive. Studies exist in literature that predict wind noise by computational methods on component level or simplified models, which are also referred as generic vehicle. For example, component level predictions are studied by [12]–[15].

According to National Aeronautics and Space Administration (NASA), prediction models for individual components do not address a total noise when individual noises of components are integrated. Instead, interaction between components must be considered. Therefore, total noise models and component noise models are different approaches and provide different feedbacks [15].

During a development program in automotive, although component level wind noise tests are common, full vehicle level wind noise is obtained after first 1:1 size representative clay model is created and tested [16]. Tests are conducted in a wind tunnel with various speeds and yaw angles. Since it is redundant to obtain wind noise inside clay model, sound measurement is obtained at far field by microphone array, which is placed away from the model.

Main purpose of wind noise testing of clay model at far field is to have quantitative value for estimation of wind noise of the vehicle to be designed. A scaled model test gives erroneous results compared to real size models, due to inconsistent ratio of wavelength and model size.

If far field aerodynamic noise was predicted without wind tunnel testing of clay model, then wind noise of the car would be obtained cheaply in early design processes. Secondly, design iterations on the vehicle surface would be fast in terms of aerodynamic noise. Similarly, early actions on solving wind noise problems would be possible.

In this thesis, automotive wind noise prediction at a far field via computational methods for a non-simplified car model will be examined. A Ford Transit Courier light commercial vehicle (LCV) model is used for wind noise prediction. Results will be compared to wind tunnel test results of the car.

Since wind noise is dominant at speeds over 100 km/h, generally 130 km/h and 140 km/h are studied. In this thesis, 130 km/h (36.1 m/s) cruising speed will be used.

1.3. Computational Aeroacoustics

In reality, aerodynamically generated noise is related to eddies in the flow. Eddies are turbulent structures of a random, non-linear and unsteady flow. Theoretically, classical acoustic analogy of Lighthill [17] emphasizes that flow creates noise itself and he classifies sources as monopole, dipole and quadrupole.

A monopole source is similar to a sink or a source that can be related to unsteady mass injection or subtraction. A boxed loudspeaker radiates sound at low frequencies like a monopole source [18]. It is a throbbing source that creates displacement of volume and efficient at low Mach flows. Its efficiency is proportional to the fourth power of velocity [18].

A dipole source consists of two co-located opposing monopoles as a combination of a source and a sink. Dipole source is a surface source. Aerodynamic loads on a vehicle surface are examples for dipole source [18]. An unboxed loudspeaker emits sound as dipoles [18]. At low speed flows, dipole is not as efficient as monopole but more efficient than quadrupole. Dipole efficiency is proportional to the sixth power of velocity [18].

Quadrupole source consists of co-located two dipoles (four monopoles) [18], which act as couple of forces; such as, turbulent flow in the wake of components of a vehicle. A tuning fork represents quadrupole source in a medium. Quadrupole efficiency is proportional to eight power of flow velocity. This is the reason why quadrupoles are highly efficient at high speed flows [18].

As a usual practice, automotive speeds mostly concern Mach number (M) around M~0.1, which is counted as low speed flow. Around M=0.1, most important monopole source is exhaust. External walls of a vehicle are the most effective dipole on it. Aeroacoustic sources are located in turbulence creator components, as shown in Figure 4. As emphasized by Zhengqi, et al. [10], the rear view mirrors and front pillars of a car are effective in wind noise. Flow separates at these regions and reattaches on side window. Reattached flow has a strong rotating motion, which causes wind noise.

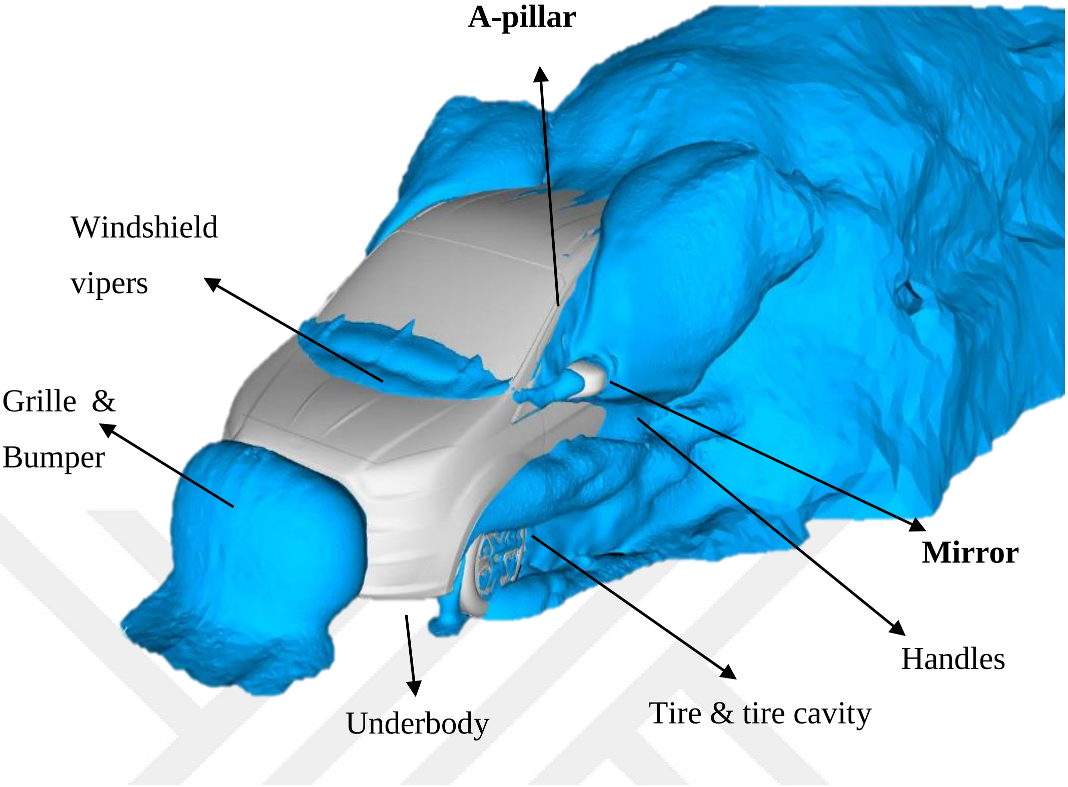

Figure 4: Wind noise sources on a car

In computational aeroacoustics (CAA), flow variables are calculated by computational fluid dynamics (CFD) simulation. CFD simulation of aeroacoustics purposes should be diverted from simulation of aerodynamics problems. While most aerodynamics problems are solved in steady state, aeroacoustics problems need unsteady solutions due to time dependent nature of sound.

Going back to Figure 3; low frequency noise is related to mechanical vibrations. It is calculated through structural equations. On contrary, wind noise consists of high frequency waves with very short wavelengths. In order to have low numerical error in CFD solution of small waves, CFD model of a real size vehicle (in this case, car model) must have more detailed mesh compared to a typical CFD mesh. In light of this reality, computational memory problem would be inevitable.

In order to decrease large memory requirement for full vehicle predictions, there are studies using component level predictions for automobile side mirror, rain gutter etc. [12]–[15], using simplified models [11], [19]–[22], [23] and full vehicles [24]. Some examples of these models are shown in Figure 5.

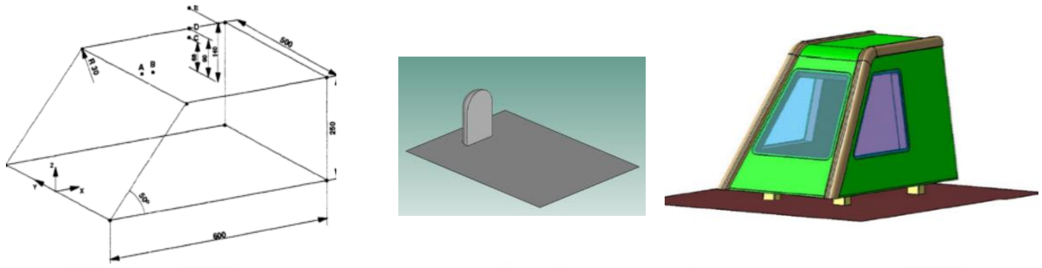

Simplified bluff body [11] Component level [14] A generic model [21]

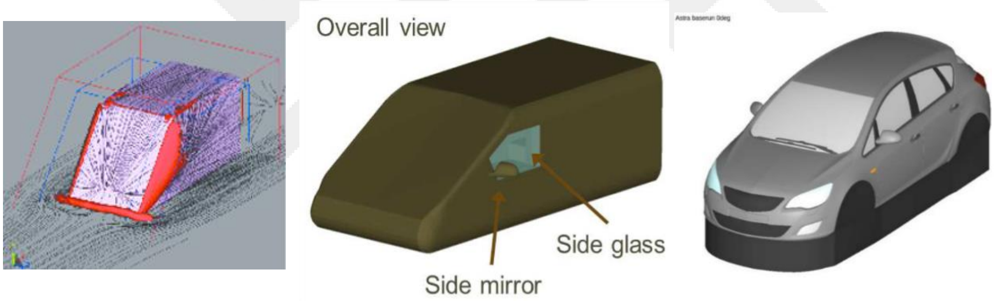

Daihatsu wedge box [22] A generic model [19],[20] Full vehicle [24]

Figure 5: Various CFD models for CAA predictions

Bergamini uses simplified bluff body for a 2D aeroacoustics application [11]. Cotoni, et al. study component level side mirror noise [14]. Blanchet, et al. and Kotapati, et al. use wedge boxes for near field aeroacoustical prediction [21][22]. Hartmann and Blanchet, et al. simulate side mirror and a-pillar on a generic model to show their interior noise contributions through a side window. [19],[20]. Also, Neuhierl, et al. use full vehicle aeroacoustical approach with structured mesh and Lattice-Boltzmann equations, using Powerflow [24]. However, this is a computationally expensive method.

Considering studies in literature, a general approach is usage of reduced models. Model reduction is fast, cheap and useful for a specific component variation comparison. However, it does not give a representative flow induced far field noise calculation of the model, which is the main point of interest of this thesis. That is why; major simplifications will not be applied in this thesis.

Combining all, modelling is done in full vehicle approach with solution of Navier-Stokes equations for unstructured mesh.

Moreover, aeroacoustic prediction methods are listed by Farassat and Casper as follows [25];

a. Fully analytical method,
b. hybrid approach,
c. semi empirical method, and
d. direct numerical method.

If the case was consisted of a simple, small model with the aim of noise prediction in near field, then (a) and (d) might be used. However, (a) and (d) are not realistic for cases of highly detailed models with huge data. Direct numerical solutions (DNS) lead to unrealistic turnaround time. Amongst these methods, (c) semi empirical method has very low error, but it needs many tests from competitor cases, thus, it is expensive.

Hybrid (zonal) method (b) splits the problem into two parts; near field evaluation using CFD and extension to far field using integral methods [26].

Main advantage of hybrid approach usage is simplicity of non-iterative, explicit equations of integral methods[11]. Hybrid methods require lower computational cost and faster solutions compared to other methods. In addition, the hybrid approach is the most common method for aeroacoustics predictions. NASA uses hybrid methods in many studies like; airframe, helicopter and propeller noise predictions [25].

As stated previously, since aerodynamically generated noise sources are composed of random, nonlinear and unsteady fluid motions, sources must be determined using accurate computation techniques [27]. Numerical error in computations includes dissipation and dispersion. Dissipation error means inaccurate amplitude calculation, whereas dispersion error is non-alignment of calculated wave frequency and actual wave frequency. To minimize these errors, higher order flow solution is needed.

A general representation of CAA methods is listed in Figure 6. Green boxes represent the selected method (porous Ffowcs Williams & Hawkings) and its higher hierarchies.

1.3.1. Hybrid Approach

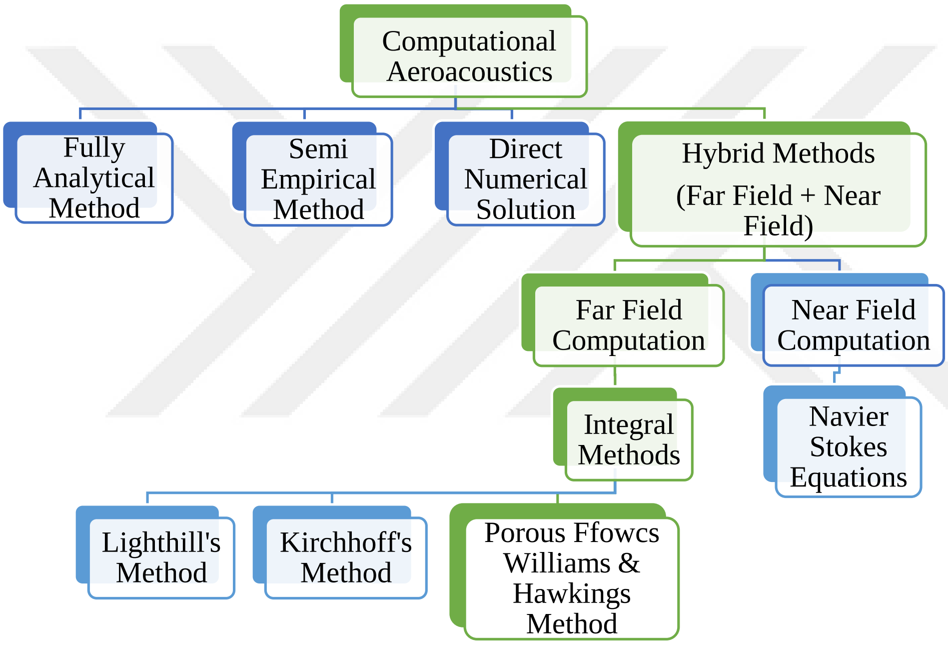

Figure 6: Methods of computational aeroacoustics

A big majority of studies in the literature use hybrid approach. Although, some of those studies use Linearized Euler Equations (LEE) [28], integral methods are the most widely used methods [12], [29]–[32].

Integral methods split the computational domain in such a way that, flow field and acoustic field are solved by different governing equations. Flow field is solved by numerical methods and acoustic field is solved by integral methods. Integral methods require nonlinearities (turbulences) in flow to be contained in a control volume (CV).

General form of integral methods follows a similar manner. Acoustic wave equation is used, which is obtained from compressible Navier-Stokes (NS) equations. Since solution of the wave equation is known, integral methods are fast and efficient.

Lyrintzis states that, there are two main approaches for integral methods, volume integral and surface integral methods [26]. Both integral methods require retarded time history of flow properties on control volume or surface from time dependent CFD simulation. Pressure fluctuations on the control surface or volume pretend as noise sources. In other words, control surface/volume becomes a cluster of sources[11]. However, one major difficulty of integral methods is accurate calculation of the retarded time effect, which requires a long record of the time history of the converged solution [26]. Then, it may lead to a storage problem. This problem may be altered by reductions in the time history. Yet, large data is inevitable. Keeping record of surface elements is more storage-efficient compared to a history of volume elements.

Since, wave propagation is defined as integrals over all sources, types of integral method impose (i) a volume integral or (ii) a surface integral of sound sources. Depending on chosen integral method, an acoustic solver program reads in acoustic source history from CFD simulation output and computes acoustic field using surface or volume integral [11].

1.3.1.1. Integral Methods

Lighthill's analogy; is a well-known volume integral method which was originally developed for unbounded flows, e.g. jet flows [33]. It is also referred as acoustic analogy or aeroacoustic analogy. The acoustic analogy is an application of CAA that reduces aeroacoustic sound sources into basic emitters.

Governing equation of Lighthill's analogy is "the wave equation" which is a rearrangement of NS equations. Since the wave equation is inconsistent around nonlinear vortex fluctuations, Lighthill's analogy strictly limits a constant flow condition in the acoustic field [4]. In other words, Lighthill's method does not allow acoustic sources or any variation of air properties in the acoustic domain. However, in application, this condition cannot always be satisfied. Solution to overcome this problem is a wider flow field and narrower acoustic field. The drawback of this solution is storage problem, which is caused by non-compact sound sources.

Another major disadvantage of the method is volume integral requirement for acoustic field solution. Due to volume integral requirement and storage problem, Lighthill's method is not actually an effective tool for the purpose of this thesis.

Still, there are many studies using Lighthill's analogy. Kumarasamy and Karbon use Lighthill-Curle equation for far field noise prediction [10], [34]. Pressure and sound intensity correlates well with experiment. Ye Li uses Lighthill's analogy and obtains consistent prediction on distribution of acoustic source [35].

There are two main surface integral methods; Ffowcs Williams–Hawkings (FW-H) Method and Kirchhoff's Method [26].

Porous FW-H Method; is an extension of Lighthill's method [36]. It is based on the same starting point of Lighthill's analogy [26]. It is also an exact rearrangement of NS equations.

Porous FW-H method takes into account the effect of moving boundaries by equivalent Huygens sources. Huygens sources consist of monopole and dipole source distributions. This method is eligible to calculate solid-surface interactions which are directly involved in flow noise generation [33].

In this method, acoustic sources are enclosed by a control surface, which is called as FW-H surface. As stated by Özyörük, sound is propagated numerically to far field by integrating FW-H equation on appropriate FW-H surface [36], [37]. Originally, FW-H method (with solid, non-porous control surface) requires volume integral; whereas, porous FW-H does not require volume integrations. Lockard states that, if the control volume is large enough to capture all non-linearity, then surface integral would be sufficient enough.

According to Lockard, non-porous FW-H method and porous FW-H method gives significantly different results in amplitude and directivity [36]. In theory of porous FW-H method, flow field calculation should be extended to uniform flow-field to predict far field wind noise with small error at low speeds [36]. In practice, this is rare.

Singer, Lockard and Lilley consider porous FW-H method as the only hybrid method [29]. Yet, it is a debatable topic as mentioned by Farassat and Casper [25]. Also, they preferred FW-H since, it can be solved in both time and frequency domain.

Kirchhoff's method; is an innovative way to aeroacoustics problems. It uses mathematical similarities between aeroacoustics and electrodynamics.

It is another surface integral method, which is very similar to FW-H method. However, Kirchhoff's method is only valid for a surface in a linear flow.

Özyörük and Long used Kirchhoff's method for ducted fan noise with a control surface in rectilinear motion [37]. Sarigul uses Kirchhoff's method for a cavity problem to a vehicle noise prediction [38].

It was proven by Lyrintzis that porous FW-H and Kirchhoff are similar [39]–[41]. However, FW-H is more robust method in terms of location and size. Results are less sensitive to control surface selection compared to Kirchhoff's method. Porous FW-H method allows non-linearity on the control surface; whereas, Kirchhoff's method assumes a solution on the surface for linear wave equation. If the solution does not satisfy the equation on surface, Kirchhoff's method provides dramatically different results.

Kirchhoff's method requires more stringent assumptions for the flow solution to reach linear part of flow field. These conditions make FW-H method more attractive.

Surface integral is storage efficient and fast compared to volume integrals. Among surface integrals, porous FW-H method is used in applications in the last 20 years. Method is shown to be equivalent to Kirchhoff's method but more robust for control surface choice, which is allowed to be porous, stationary, and non-deforming.

1.4. Frequency Limitation

Good aeroacoustical predictions on a generic vehicle model are made by Hartmann in [20] for a frequency interval between 200 Hz - 2500 Hz. The vehicle is composed of a rectangular box with a wedge in front. Furthermore, a rearview side mirror and a side window are included in its model. Four different prediction methods are used.

Three out of four methods have incompressible DES turbulence modeling. The remaining one uses Lattice Boltzmann with weak compressibility. All four models have good correlation with experiment between 200-2500 Hz. Frequencies below 200 Hz and above 2500 Hz encounter deviations between experiment and prediction due to limitations of modelling and assumptions. Similar to this example, most CAA studies disregard frequency spectrum below a certain frequency. Another example is Fink's study [13], which ignores frequencies up to 200 Hz. Considering four successful approaches of Hartmann in [20]; mesh size, time step, physical simulation time and targeted frequency interval are used as beginning points of this thesis. These assumptions will be discussed in Methodology chapter with other assumptions.

1.5. Flow Simulation

In this section, solution methods of CFD simulation are discussed. Mathematical details of solutions will be given in Methodology chapter.

Vehicle model is simulated using the commercial software FLUENT which is used by many aerodynamics and aeroacoustics studies. Some examples are as follows; general aeroacoustics solution by Kim, et al. in [42], rearview mirror aeroacoustics contributions by Hendriana, et al. in [43], cavity noise of sunroof is studied by Grace in [44] and noise generated by a car rain-gutter is inspected by Kim, et al in [9].

As mentioned before, wave equation is used for linear wave propagation in acoustic field. Contrarily, NS equations define fluid motion in flow field to solve highly detailed turbulence eddies. However, DNS for a non-simplified car model exceeds capabilities of high power computers.

Unsteady Reynold Averaged Navier-Stokes (RANS) simulation is an alternative for turbulence modelling. It is based on time averaging of NS equations. A wide variety of automotive aeroacoustics applications use RANS based unsteady simulation. Yang, et al. studied on side window buffeting [45], Hayes, et al. worked on exhaust gas treatment [46] and Tu, et al. have studies on external aeroacoustics, heat transfer and flow acoustics of Heating, Ventilating and Air Conditioning (HVAC) units [47]. Alas, time averaging that is used by unsteady RANS, results in loss of unsteadiness in small turbulence structures [48]. Cengiz and Özyörük state that; since aerodynamic noise generation problems depend on unsteadiness, URANS method is insufficient for aeroacoustics problems [48]. Also, URANS solutions are not sufficient for unsteady flows with large eddies [27], [49]. Large Eddy Simulation (LES) avoids this problem. Contrary to time averaging employed by unsteady RANS, volumetric averaging is applied by LES. Large eddies are directly solved and small eddies are modelled [50]. Therefore, drawback of LES is high computing cost for boundary layer solution [50].

RANS and LES simulations are combined in Detached Eddy Simulation (DES) method by Spalart [51]. This method uses RANS modeling in the wall boundary layer region and applies LES for regions outside the boundary layer. By this hybridization, computing needs are reduced without loss in accuracy. One disadvantage of DES is less eddy viscosity development [27]. For some cases, DES might resolve less eddy viscosity than the actual value. Main problem of DES is that LES mode can be activated inside boundary layer, if thickness of the boundary layer is somehow larger than parallel grid spacing to the wall [27]. Thus, LES method cannot model velocity fluctuations inside the boundary layer. To overcome activation problem, a modified version of DES is also available. Delayed Detached Eddy Simulation (DDES) limits length scale by an eddy viscosity field in order to delay LES mode transition [52]. Since DDES is combination of RANS and LES, mathematical description is given in Methodology chapter under RANS and LES modelling details.

Furthermore, general automotive speeds are around 0.1 Mach, which can be treated as incompressible. In this thesis, flow speed is taken as 36.1 m/s (0.1 M) and flow is assumed as incompressible. Kato states that, if primary target of a method is to predict broadband noise, incompressible flow assumption is valid for automotive speeds [4]. In other words, drawback of incompressible flow assumption is problem of predicting specific peaks. Contrarily, incompressible flow field is used by Hartmann [20]. According to him, total pressure is dominated by incompressible part of flow. Since unsteady sources require large data to store, incompressible flow assumption relaxes problem without significant effect.

By nature, the acoustic waves are non-dissipative and non-dispersive. Thus, higher order discretization is crucial for solutions with low-dissipation and low-dispersion. 2nd order central discretization is preferred in some aeroacoustics applications [9], [10], [12]. Whereas, many applications include higher order discretization; [11] uses 3rd order, [27] uses 4th order. On the other hand, many studies avoid non-central schemes, which produce dissipation. FLUENT has 3rd order MUSCL discretization (Monotone Upstream-Centered Schemes for Conservation Laws). It is a blend of central differencing and second order upwind. It is effective compared to second order schemes. Spatial gradient is also important. Least Square Cell Based gradient is recommended by FLUENT for accurate flow solution [53]. It is effective for polyhedral meshes. For triangular meshes, stability problem may occur [53]. Since triangular mesh is used in this thesis, Green-Gauss Node-Based gradient evaluation is preferred.

1.6. The Objectives of the Thesis

The objective of the thesis is to compute far field aerodynamic noise radiated from an automobile using solutions of Navier-Stokes and Ffowcs Williams & Hawkings equations. Expected achievements from this implementation process are listed as follows;

- Accurate, 3D, unsteady CFD simulation for a low Mach flow,
- Good alignment of broadband flow noise between its prediction and test results in a frequency interval of 200 Hz and 2500 Hz,
- Practicality, i.e. adequate turnaround time, even for a detailed model.

1.7. The Scope of the Thesis

Combining the discussions so far, wind noise prediction is aimed for a real, non-simplified CFD model of an automobile up to a frequency of 2.5 kHz. Ford Transit Courier is used as the car model. The CAA method is selected as porous FW-H method, which is a hybrid integral method. It consists of two parts; CFD simulation and FW-H integration. The CFD simulation is aimed to be unsteady, incompressible and three-dimensional. Turbulence modelling is used as DDES. Spatially 3rd order MUSCL discretization and temporally 2nd order implicit discretizations are used for numerical calculations of solver FLUENT. The FW-H integration is employed by a FORTRAN code. The code is aimed to be capable of calculating aerodynamically generated noise at far field with success.

In Chapter 2, methodology of the thesis is presented. First, governing equations of the flow are expressed. Then, solver is briefly introduced. Spatial and temporal discretizations are discussed. After boundary conditions of the model are given, model details are introduced. Implementation of the FW-H integration into the post-process of CFD simulation is given. Finally, wind tunnel test conditions are shown.

In Chapter 3, results of the whole process are introduced. At first, validations of steady and unsteady CFD simulations are given in terms of mesh independence and convergence studies. These are followed by aerodynamical verification by a brief introduction and discussion on obtained drag and pressure coefficients, C_D and C_p, respectively. Then, various Q-Criterion of the model are compared for source characterization. FW-H integration code is tested with a monopole source and comparison between computed and analytical results is presented. In the end, calculated far field sound pressure levels are plotted with respect to test result.

In Chapter 4, conclusion and comments on the thesis are provided. Future work and planned actions on the subject are presented.

CHAPTER 2

METHODOLOGY

In this chapter, background information is given for flow solutions and far field calculations. Governing equations of the flow, details of the solver (gradient calculation equations and discretization methods which are embedded in FLUENT software) are provided. Then, boundary conditions are followed. CFD simulation model details are then presented. Far field propagation model, i.e. FW-H equation is given. Finally wind tunnel testing is discussed in the last section of this chapter.

2.1. Governing Flow Equations

Aforementioned methodology for flow solution consists of unsteady, incompressible, three dimensional CFD simulation with Delayed Detached Eddy Simulation (DDES) modelling. The related governing equations are given in this chapter.

DDES turbulence modelling is an extension of DES turbulence modelling. Meanwhile, DES is a combination of Reynolds-Averaged Navier-Stokes (RANS) and Large Eddy Simulation (LES) methods. Corresponding equations of RANS and LES are given separately. Further details on DDES model are also given.

2.1.1. Reynolds-Averaged Navier-Stokes Equations

Equation 1 and Equation 2 show time dependent, incompressible, three dimensional incompressible RANS equations in Cartesian coordinates.

$$\frac{\partial u_i}{\partial x_i} = 0 \qquad (1)$$

$$\frac{\partial u_i}{\partial t}+\frac{\partial}{\partial x_j}\left(u_i u_j\right)$$

$$=-\frac{1}{\rho}\frac{\partial p}{\partial x_i}+\frac{\partial}{\partial x_j}\left[\frac{\mu}{\rho}\left(\frac{\partial u_i}{\partial x_j}+\frac{\partial u_j}{\partial x_i}-\frac{2}{3}\delta_{ij}\frac{\partial u_l}{\partial x_l}\right)\right] \tag{2}$$

$$-\frac{\partial}{\partial x_j}\left(-\overline{u_i' u_j'}\right)$$

where bar sign denotes time average and prime sign stands for fluctuations. The term, $\tau_{ij}=-\overline{u_i' u_j'}$ is Reynolds stress tensor. Additionally, μ is molecular viscosity.

Considering the RANS equations above, system of equations is not yet closed. Spalart-Allmaras, $k-\omega$ model or $k-\epsilon$ model are used for closure equations. Furthermore, all these models employ the Boussinesq hypothesis to relate Reynolds stresses τ_{ij} to the mean velocity gradients. The Boussinesq hypothesis is given by;

$$-\overline{u_i' u_j'}=2\frac{\mu_T}{\rho}S_{ij}-\frac{2}{3}k\delta_{ij} \tag{3}$$

where S_{ij} is the mean strain-rate tensor, which reads,

$$S_{ij}=\frac{1}{2}\left(\frac{\partial u_i}{\partial x_j}+\frac{\partial u_j}{\partial x_i}\right) \tag{4}$$

where μ_T is eddy viscosity. It is defined variably in turbulence models.

Although, there are several turbulence models, $k-\epsilon$ fits well for fully turbulent flows. Compared to $k-\omega$ model, $k-\epsilon$ model is better in separated shear layer flows [53].

2.1.1.1. Standard k-ϵ Model

Modeling is based on turbulence kinetic energy and its dissipation rate, k and ϵ. Flow is assumed as fully turbulent and molecular viscosity effects are neglected. In other words, standard $k-\epsilon$ model is only valid for fully turbulent flows [53].

Eddy viscosity is defined as,

$$\mu_T = \rho C_{\mu} k^2/\epsilon \tag{5}$$

The turbulence kinetic energy is obtained from transport equation, which reads,

$$\begin{aligned} \frac{\partial}{\partial t}(k) + \frac{\partial}{\partial x_i}(k u_i) \\ &= \frac{1}{\rho}\frac{\partial}{\partial x_j}\left[\left(\mu + \frac{\mu_T}{\sigma_k}\right)\frac{\partial k}{\partial x_j}\right] - \epsilon \\ &+ \frac{1}{\rho}(G_k + G_b + Y_M + S_k) \end{aligned} \tag{6}$$

Similarly, rate of dissipation of k is governed by,

$$\begin{aligned} \frac{\partial \epsilon}{\partial t} + \frac{\partial}{\partial x_i}(\epsilon u_i) \\ &= \frac{1}{\rho}\frac{\partial}{\partial x_j}\left[\left(\mu + \frac{\mu_T}{\sigma_\epsilon}\right)\frac{\partial \epsilon}{\partial x_j}\right] + \frac{1}{\rho} C_{\epsilon 1}\frac{\epsilon}{k}(G_k + C_{\epsilon 3} G_b) \\ &- C_{\epsilon 2}\frac{\epsilon^2}{k} S_\epsilon \end{aligned} \tag{7}$$

Values of closure coefficients are,

$$C_{\epsilon 1} = 1.44, \quad C_{\epsilon 2} = 1.92, \quad C_\mu = 0.09, \quad \sigma_k = 1.0, \quad \sigma_\epsilon = 1.3 \tag{8}$$

These constants have been determined from experiments for fundamental turbulent shear flows. FLUENT’s user’s guide document [53] states that these constants work adequately for a wide range of wall-bounded and free shear flows.

In above equations, G_k is production of turbulence kinetic energy due to mean velocity gradients, which is expressed as,

$$G_k = -\rho \overline{u_i' u_j'} \frac{\partial u_j}{\partial x_i} \tag{9}$$

Likewise, G_b is generation of turbulence kinetic energy from buoyancy,

$$G_b = \beta g_i \frac{\mu}{\mathrm{Pr}_t} \frac{\partial T}{\partial x_i} = 0 \tag{10}$$

where Pr_t is turbulent Prandtl number and g_i are gravity vector components. The $k - \epsilon$ models use a default value of Pr_t as 0.85. Similarly, the buoyancy term is given by;

$$\beta = -\frac{1}{\rho}\left(\frac{\partial \rho}{\partial T}\right)_p = 0\ (incompressible\ flow) \tag{11}$$

Also, $C_{3\epsilon}$ term includes buoyancy effect on ϵ. Following relation represents the way FLUENT calculates $C_{3\epsilon}$,

$$C_{3\epsilon} = tanh\left|\frac{v}{u}\right| \tag{12}$$

In $k - \epsilon$ turbulence model, Y_m is dilatation dissipation. It is the contribution of compressibility on turbulence. Obviously, it is neglected by incompressible flows. Also, S_k and S_ϵ are user defined source terms. In this case these are ignored.

2.1.1.2. Realizable k-ϵ Model

Realizable $k - \epsilon$ model consists of a new formulation for turbulent kinetic energy and its dissipation rate. It is an improved version of standard $k - \epsilon$ model. It performs well for a variety of flows, that involve rotation, boundary layers under strong adverse pressure gradients, separation and recirculation.

In standard $k - \epsilon$ model, if mean strain rate is large enough, normal stress becomes negative (by definition, it should be positive). Realizable model is proposed by Shih, et al. [54]. In this model, normal stress is made positive by C_μ, which is,

$$C_\mu = \frac{1}{A_0 + A_s \frac{kU^*}{\epsilon}} \tag{13}$$

U^* is given in Equation 14 and $\widetilde{\Omega_{ij}}$ is given in Equation 15. Here, the rotating reference frame with angular velocity of ω, mean rate of rotation tensor is showed as $\overline{\Omega_{ij}}$.

$$U^* = \sqrt{S_{ij}S_{ij} + \widetilde{\Omega_{ij}}\widetilde{\Omega_{ij}}} \tag{14}$$

$$\widetilde{\Omega_{ij}} = \overline{\Omega_{ij}} - \epsilon_{ijk}\omega_k \tag{15}$$

The model constants A_0 and A_s are given by,

$$A_0 = 4.04\,, \qquad A_s = \sqrt{6}cos\varphi \tag{16}$$

The constants are defined as follows,

$$\begin{gathered}\varphi = \frac{1}{3}\cos^{-1}\left(\sqrt{6}W\right), \qquad W = \frac{S_{ij}S_{jk}S_{ki}}{\tilde{S}^3}, \qquad \tilde{S} = \sqrt{S_{ij}S_{ij}}, \\ S_{ij} = \frac{1}{2}\left(\frac{\partial u_i}{\partial x_j} + \frac{\partial u_j}{\partial x_i}\right)\end{gathered} \tag{17}$$

Realizable $k - \epsilon$ model employs transport equations for k and ϵ, which reads,

$$\begin{aligned}\frac{\partial k}{\partial t} + \frac{\partial}{\partial x_j}\left(ku_j\right) &\\ &= \frac{1}{\rho}\frac{\partial}{\partial x_j}\left[\left(\mu + \frac{\mu_T}{\sigma_k}\right)\frac{\partial k}{\partial x_j}\right] - \epsilon \\ &+ \frac{1}{\rho}\left(G_k + G_b + Y_M + S_k\right)\end{aligned} \tag{18}$$

$$\begin{aligned}\frac{\partial \epsilon}{\partial t} + \frac{\partial}{\partial x_j}\left(\epsilon u_j\right) &\\ &= \frac{1}{\rho}\frac{\partial}{\partial x_j}\left[\left(\mu + \frac{\mu_T}{\sigma_\epsilon}\right)\frac{\partial \epsilon}{\partial x_j}\right] + C_1 S\epsilon - C_2\frac{\epsilon^2}{k + \sqrt{\frac{\mu}{\rho}\epsilon}} \\ &+ \frac{1}{\rho}C_{\epsilon 1}\frac{\epsilon}{k}C_{\epsilon 3}G_b + \frac{1}{\rho}S_\epsilon\end{aligned} \tag{19}$$

the other constants are defined as follows,

$$C_1 = \max\left[0.43, \frac{\eta}{\eta+5}\right], \quad \eta = S\frac{k}{\epsilon}, \quad S = \sqrt{2S_{ij}S_{ij}} \tag{20}$$

The model constants $C_{\epsilon 3}$, G_k and G_b are expressed below and Y_M, S_k and S_ϵ are neglected.

$$C_{\epsilon 1} = 1.44, \quad C_2 = 1.9, \quad \sigma_k = 1.0, \quad \sigma_\epsilon = 1.2 \tag{21}$$

2.1.2. Large Eddy Simulation Model

Direct numerical solution (DNS) does not require modelling. Instead, turbulence eddies are resolved directly. However, it is not practical for flows with high Reynolds number. On the other hand, large eddies cannot be resolved by RANS. Large Eddy Simulation (LES) model emerges as a compromise between DNS and RANS. It is a combination of direct solution of large eddies and modelling of small eddies via subgrid-scale model (SGS) [49]. As stated by Khan, LES can be represented as a combination of resolved velocity field and subgrid field, whose effect on resolved velocity field is obtained by SGS [50]. Advantage of LES is ability to resolve larger eddies [50]. These are directly affected by geometry and boundary conditions. On the contrary, small eddies are less geometry dependent and isotropic.

Unsteady Navier-Stokes equations are filtered to obtain governing equations of LES. Filtering process filters eddies out whose scales are smaller than the filter width.

FLUENT uses finite-volume discretization to provide filtering implicitly. Filtered, incompressible NS equations in Cartesian coordinates are governed by,

$$\frac{\partial \bar{u}_i}{\partial x_i} = 0 \tag{22}$$

$$\frac{\partial \bar{u}_i}{\partial t} + \frac{\partial}{\partial x_j}\left(\bar{u}_i\bar{u}_j\right) = -\frac{1}{\rho}\frac{\partial \bar{p}}{\partial x_i} + \frac{\partial}{\partial x_j}\left(\frac{\mu}{\rho}\sigma_{ij}\right) - \frac{\partial \tau_{ij}}{\partial x_j} \tag{23}$$

Here, overbar denotes filtered variables and, σ_{ij} is called as stress tensor, which reads,

$$\sigma_{ij} = \left(\frac{\partial \bar{u}_i}{\partial x_j} + \frac{\partial \bar{u}_j}{\partial x_i}\right) - \frac{2}{3}\delta_{ij}\frac{\partial \bar{u}_l}{\partial x_l} \tag{24}$$

$$\tau_{ij} = \overline{u_i u_j} - \bar{u}_i \bar{u}_j \tag{25}$$

where τ_{ij} is subgrid-scale stress, which is unknown. It is product of filtering and need to be modeled. FLUENT employs Boussinesq hypothesis for subgrid-scale stress as,

$$\tau_{ij} - \frac{1}{3}\tau_{kk}\delta_{ij} = -2\mu_t \bar{S}_{ij} \tag{26}$$

The term, μ_t is eddy viscosity at subgrid-scale. Secondly, τ_{kk} represents isotropic definition of the subgrid-scale stresses.

Similar to RANS, rate of strain tensor for resolved scale is given as,

$$\bar{S}_{ij} = \frac{1}{2}\left(\frac{\partial \bar{u}_i}{\partial x_j} + \frac{\partial \bar{u}_j}{\partial x_i}\right) \tag{27}$$

Eddy viscosity is defined in Smagorinsky-Lilly subgrid-scale modelling, which reads,

$$\mu_T = \rho L_s^2 |\bar{S}| \tag{28}$$

$$|\bar{S}| = \sqrt{2\overline{S_{ij}}\,\overline{S_{ij}}} \tag{29}$$

Also, L_s is mixing length for subgrid scales, which is represented by,

$$L_s = \min\left(\kappa d, C_s V^{1/3}\right) \tag{30}$$

where the von Karman constant is symbolized as κ. The closest wall distance is represented as d. Also, Smagorinsky constant is shown as C_s, whose default value is 0.1 in FLUENT. Finally, V represents the volume of computational cell.

2.1.3. Delayed Detached Eddy Simulation

The DDES modelling has been introduced in Section 2.1.3. A length scale limiter delays RANS to LES transition. The length scale limiter is defined as,

$$\tilde{d} = \min(d, C_{des}\Delta x) \tag{31}$$

where, isotropic turbulence decay calibration is shown by empirical constant C_{des}, typically as 0.65. Also, Δx is the largest grid spacing in Cartesian coordinates.

DES model defines the length scale, d, as distance to closest wall. It is replaced by a new length scale, $\tilde{d}$, everywhere on the domain. The length scale $\tilde{d}$ is given by,

$$\tilde{d} = d - F_d max(0, d - C_{des}\Delta x) \tag{32}$$

and, other terms are represented as follows;

$$F_d = 1 - \tanh((8r_d)^3) \tag{33}$$

$$r_d = \frac{\nu_t + \nu}{\sqrt{\frac{\partial u_i}{\partial x_j}\frac{\partial u_i}{\partial x_j}}\kappa^2 d^2} \tag{34}$$

where, ν and ν_t are molecular kinematic viscosity and turbulent kinematic viscosity.

2.2. Solver Type

FLUENT offers two solver types. Density based solver can only be used for compressible flow. Pressure based solver is appropriate for incompressible flow.

In terms of pressure and velocity coupling, FLUENT offers two coupling methods. Segregated method is robust, while coupled method is appropriate for unsteady flows. Coupled algorithm solves continuity and momentum equations simultaneously, while segregated method solves them separately. Coupled method is more accurate and converges faster compared to segregated method. Thus, coupled method is used in this thesis.

2.3. Gradients

Gradients are calculated by Green-Gauss Node-Based evolution. Simply, it is average of values at nodes of a cell. Total number of faces is represented as N_f.

$$\bar{\alpha}_f = \frac{1}{N_f} \sum_{n}^{N_f} \bar{\alpha}_n \tag{35}$$

where, α_f is a variable on a cell face f and α_n is a flow variable at n^th node of a cell.

2.4. Discretization

High orders of discretization are required for aeroacoustic calculations with low dissipation and low dispersion error. FLUENT offers maximum third order scheme.

2.4.1. Spatial Discretization

Monotone Upstream-Centered Schemes for Conservation Laws (MUSCL) is a mixture of second order central differencing and second order upwind schemes. Spatial discretization on computational domain is shown in Figure 7.

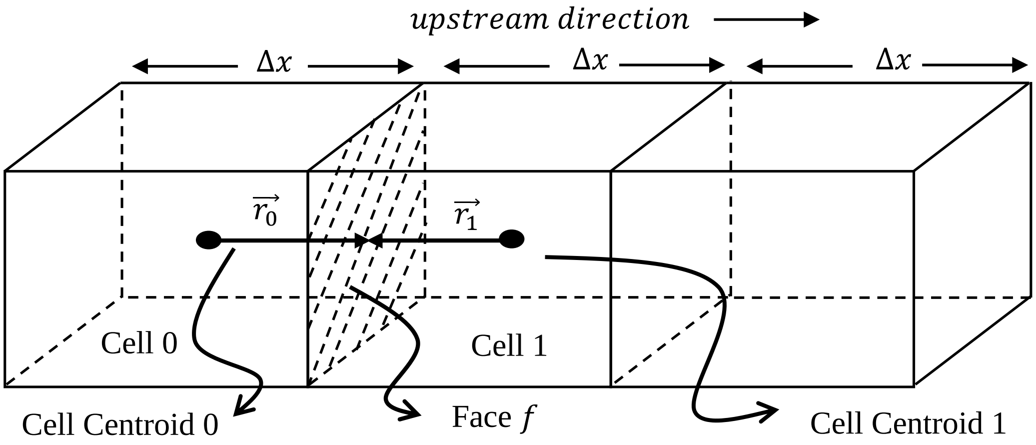

Figure 7: Spatial discretization on the computational domain

Here, the MUSCL combination calculates a variable α_f on a face f as,

$$\alpha_f = \Psi \alpha_{f,CD} + (1 - \Psi)\alpha_{f,SOU} \tag{36}$$

where, $\alpha_{f,CD}$ represents a quantity of the face f that is found from central differencing and $\alpha_{f,SOU}$ is a quantity that is obtained from second order upwind. When dummy constant is used as $\Psi = 0$ in above equation, it becomes exactly a central difference discretization. Similarly, $\Psi = 1$ makes the equation completely second order upwind equation. FLUENT uses $\Psi = 0.5$ as a default value for combination.

The central differencing part of MUSCL scheme is found as,

$$\alpha_{f,CD} = 1/2 * (\alpha_0 + \alpha_1) + 1/2 * (\nabla\alpha_0 \cdot \overrightarrow{r_0} + \nabla\alpha_1 \cdot \overrightarrow{r_1}) \tag{37}$$

The subscripts 0 and 1 refer to cells with common face f. Likewise, α represents a quantity of the upstream cell from its cell center and $\nabla\alpha$ means its gradient. Similarly, gradients $\nabla\alpha_0$ and $\nabla\alpha_1$ are located at cells 0 and 1. The $\overrightarrow{r_0}$ and $\overrightarrow{r_1}$ terms are the vectors that are defined from centroids of the cells and directed towards the centroid of faces.

Second order upwind part of MUSCL combination is obtained through,

$$\alpha_{f,SOU} = \alpha_1 + \nabla\alpha_1 \cdot \overrightarrow{r_1} \tag{38}$$

$\nabla\alpha$ terms at cell centers in the equations are computed by divergence theorem;

$$\nabla\alpha = \frac{1}{V} \sum_{f}^{N_{faces}} \tilde{\alpha}_f \vec{A} \tag{39}$$

where V is cell volume and $\vec{A}$ is area vector of common face f. Summation is made over all neighbor cells. In this equation, $\tilde{\alpha}_f$ term is the α value at face centroid of f.

2.4.2. Temporal Discretization

Transient simulations need both spatial and temporal discretization. Discretization in space is similar for both transient and steady simulations. Since incompressible flow is assumed, explicit discretization is not possible. Thus, bounded second order implicit temporal discretization is used. It is represented as,

$$\frac{3\alpha^{n+1} - 4\alpha^{n} + \alpha^{n-1}}{2\Delta t} = F(\alpha^{n+1}) \tag{40}$$

2.5. Boundary Conditions

Model consists of wall, velocity-inlet, pressure-outlet, symmetry zone as boundary conditions, which are shown in Figure 8 and Figure 9.

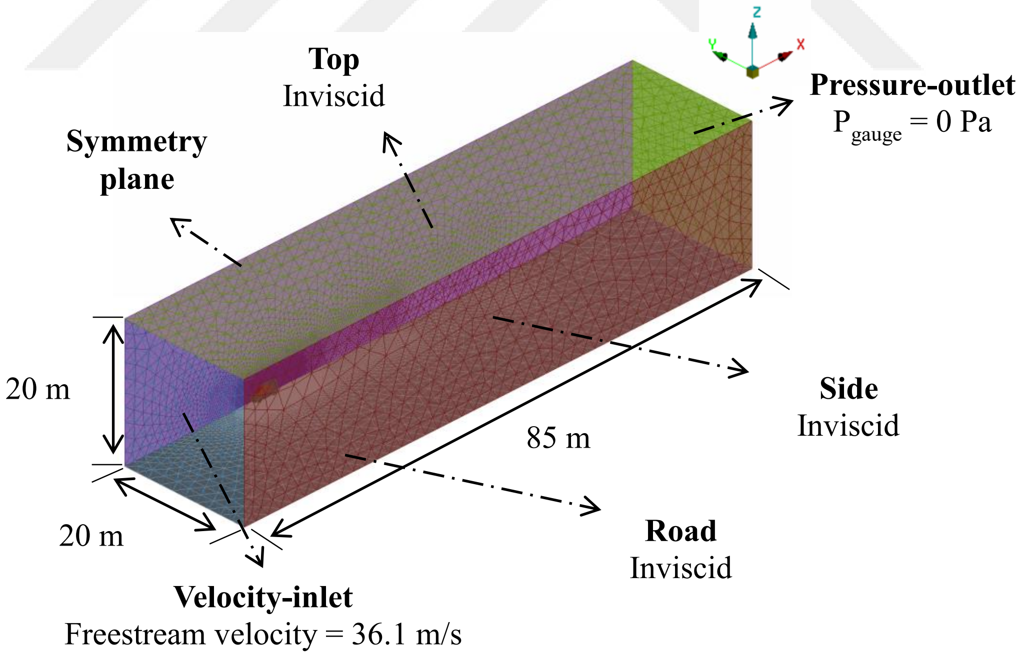

Figure 8: Boundary conditions of the model

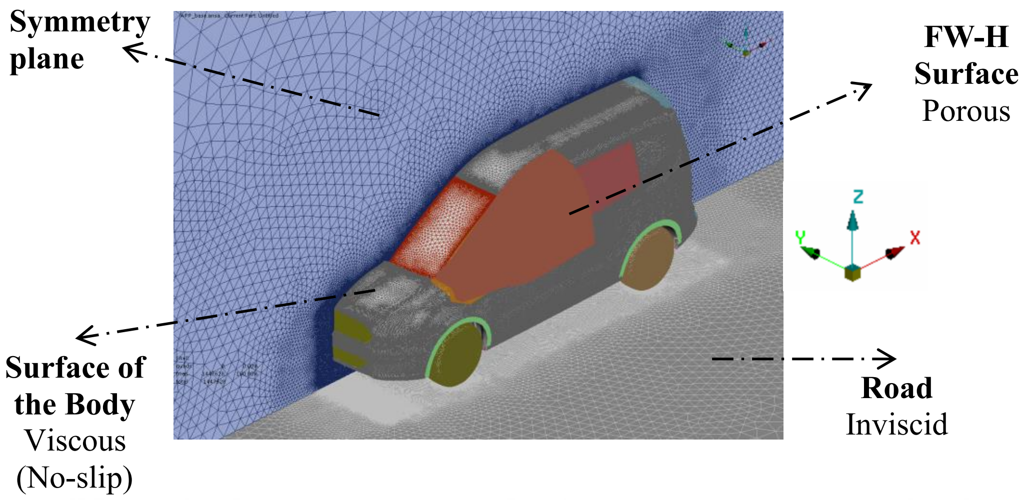

Figure 9: Model geometry

2.5.1. Wall Boundary Conditions

Vehicle surface, road and far field conditions are defined as wall boundary condition type zone. Road and far field walls are inviscid; so that, boundary layer is not modelled. Contrarily, vehicle surface is viscous wall with no-slip condition, i.e. normal and tangential velocity components on the walls are zero. Also, normal derivative of pressure from the momentum equation becomes zero as well.

$$\nabla p \cdot \tilde{n} = 0 \tag{41}$$

Additionally, viscous wall surfaces do not have turbulence terms,

$$\mu_t = 0 \tag{42}$$

2.5.2. Velocity-Inlet Boundary Conditions

Inflow surface is velocity-inlet type boundary condition with inlet flow as 36.1 m/s.

Reynolds number is calculated as ~10^7 using following properties;

- Velocity: 36.1 m/s,
- Density: 1.225 kg/m^3,
- Dynamic viscosity: 1.789 x10^{-5} kg/m/s and
- Characteristic length, used as 4 m (vehicle length).

2.5.3. Pressure-Outlet Boundary Conditions

Outflow surface is defined as pressure-outlet type boundary condition. The gauge (static) pressure is specified as 0 Pa at this zone.

2.5.4. Symmetry Boundary Condition

Vehicle is modeled in half with a symmetry boundary condition on its longitudinal axis. By applying this boundary condition, vehicle is assumed to be symmetrical which is quite true for most cases. Thus, computational cost is decreased without significant effect. This boundary condition is used when the surface of the body and presumed pattern of the solution have mirror symmetry. The no slip condition is not applicable on this surface. It is assumed as an inviscid surface.

2.6. Model Details

In this thesis, two approaches are used for modelling of the vehicle in CFD simulations to simulate conditions of the tested vehicles. Unfortunately, wind tunnel test is not a combined test with aerodynamic & aeroacoustics calculations. There are two different test setups in Ford Otosan database. Both tests were done in Ford Merkenich Wind Tunnel. Test conditions will be discussed in the Section 2.8. In a brief summary, the first test aims to calculate drag coefficient (C_D) of the vehicle, but does not contain acoustic testing. Similarly, second test only cares for wind noise of the vehicle.

The first test is simulated with a modelling approach to represent aerodynamical properties of the *aerodynamically tested vehicle*. Similarly, another modelling approach is used to simulate aeroacoustics of the vehicle that was *tested aeroacoustically*. From this point forth, models of first and second approaches will be referred as "**Base Model**" and "**Aeroacoustics Model**", respectively. Since, aeroacoustics model is not verified aerodynamically in tests, base model is only used for aerodynamical verification of aeroacoustics model. These results will be further discussed in Section 3.2

In order to capture aerodynamical characteristics of the tested vehicle, the base model is in 'on road condition' with additional taped flushness gaps as shown in Figure 10.

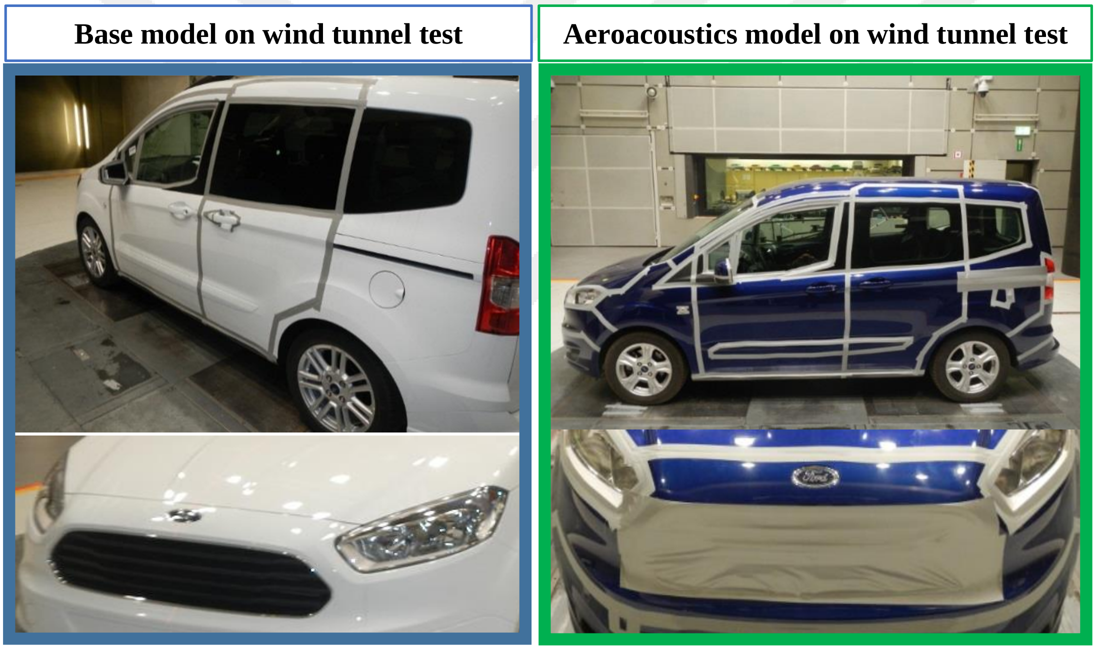

Base model on wind tunnel test

Aeroacoustics model on wind tunnel test

Figure 10: Test conditions of base model (left) and aeroacoustics model (right)

Furthermore, in order to decrease required computational power in aeroacoustics calculations, some geometric features are disregarded in the aeroacoustics model as well as aeroacoustic wind tunnel test. Geometric feature simplifications on the aeroacoustic wind tunnel test are displayed in Figure 10. It is assumed that the disregarded features do not contribute much on vehicle wind noise. In other words, these regions are not primary aeroacoustical sources. Disregarded features can be itemized as follows;

- Front grille opening is closed with duct tape, see Figure 11,
- Speed lip is removed, see Figure 11,
- Bumper is simplified by taping the fog lamps and gaps, see Figure 11,
- Considering underbody of a car is acoustically effective at low frequencies, as stated by Her, et al. [55] and Powell, et al. [56]. Also, bottom of the vehicle is assumed as smooth, i.e. smoth engine bay, no exhaust, no fuel tank, no spare tire and all features over floor panel are disregarded. see Figure 11.

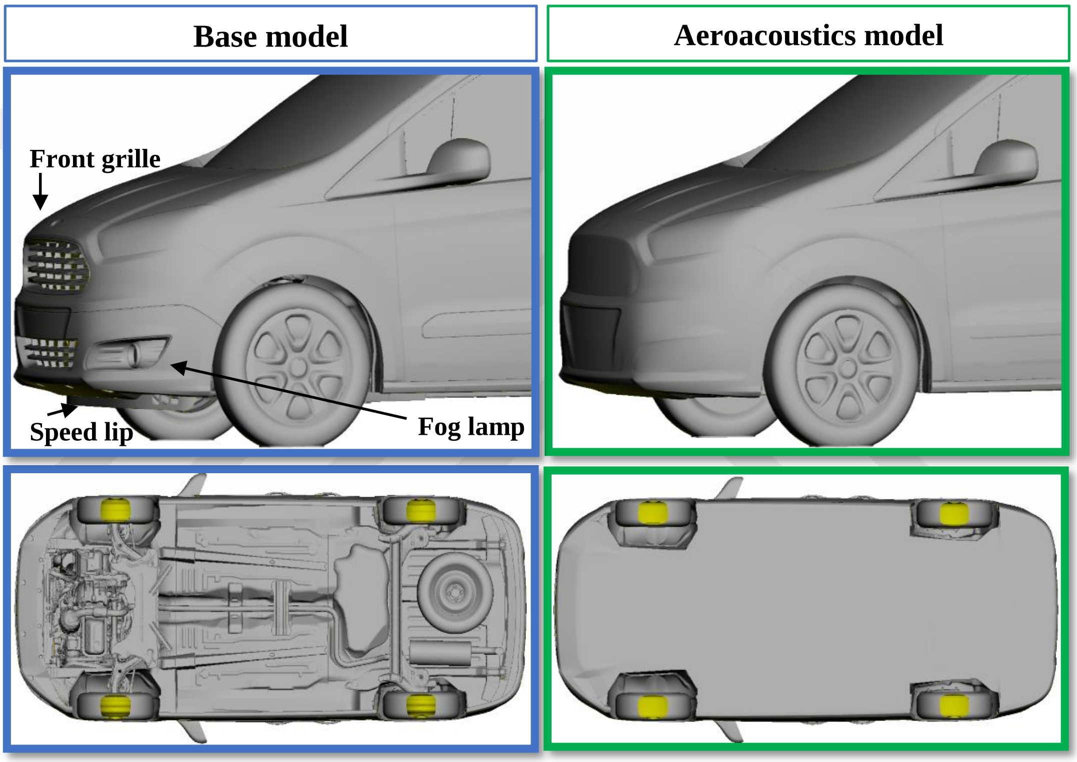

Figure 11: Applied geometric features to represent test conditions

2.6.1. Aeroacoustics Model Details

Ideally, whole model should be contained in the FW-H surface. However, vehicle model is not aimed to be reduced. The only reduction is simplification of large gaps on aeroacoustics model, which is also simplified by applying duct tapes on wind tunnel test. Furthermore, FW-H surface placement is crucial due to its additional meshes that leads to larger data size. In order to have a model that is within practical computational limits, FW-H surface is placed around **main wind noise contributors** (i.e. side mirror and a-pillar) on a Ford Transit Courier vehicle. It is initially assumed that, keeping all major noise creator regions in the FW-H surface and getting their contribution on far field noise would be sufficient for capturing wind noise level of the whole vehicle.

As seen from Figure 12, FW-H surface (in light brown) covers side mirror, A-pillar, side window, door-beltline and part of windshield. The FW-H surface is closed, with one side on vehicle and the other side away from the surface of the vehicle.

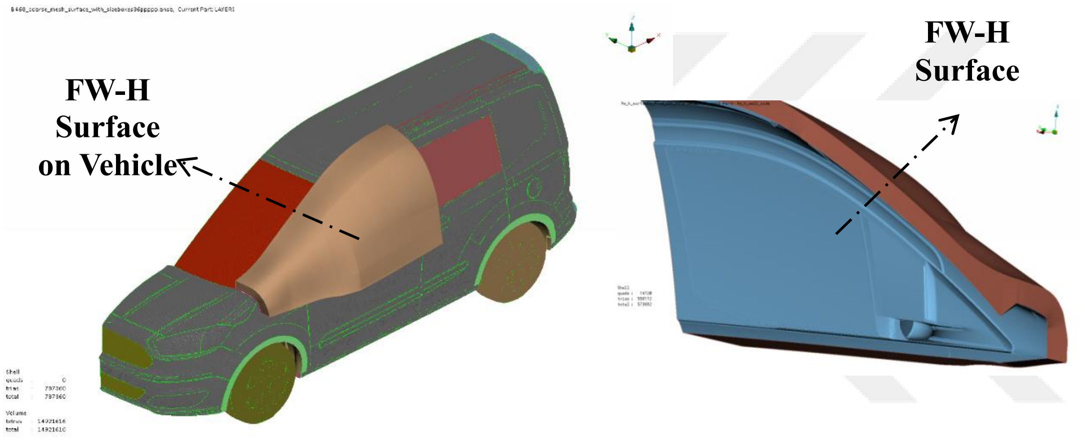

Figure 12: FW-H surface on aeroacoustics model

2.6.2. Spatial and Temporal Resolutions

Maximum frequency to be resolved is limited by spatial resolution, mostly. Keith, et al. state that, 1/8 of a wavelength should be used for number of grid spacing to resolve a wave, when fourth-order spatial discretization is used [57]. In this thesis, spatial resolution is a combination of two 2nd order schemes, FLUENT interprets it as a third order scheme. Therefore, 20 grid spacing are sufficient to resolve a 136 mm wave (for 2.5 kHz). Also, Khan uses 10 grids per wave for a 4th order solver [50].

On the other hand, temporal discretization is implicit. Hence, Courant-Friedrichs-Lewy (CFL) calculations are redundant.

2.6.2.1. Spatial Resolution

Objective of this thesis underlines prediction up to a frequency of 2.5 kHz. Required number of grids to resolve one acoustic wave is proposed by Khan as 10 points per wavelength [50]. Also, Her and Coney used 1/8 of a wavelength for number of grids per wave [55]. This would make 17 grids per wave, if the maximum frequency was used as 2.5kHz with this selection. However, this study uses 4th order spatial solver. Since 3rd order solver is used in this thesis, 20 grids per wavelength is sufficient. In Table 1, maximum frequencies to be achieved with respect to number of grids to resolve a sound wave is shown. In this table, wavelengths of sound waves are denoted as λ. Table shows spatial resolution as maximum mesh size, which is calculated by dividing wavelength by number of grids.

Table 1: Spatial resolution vs maximum frequency and number of grids

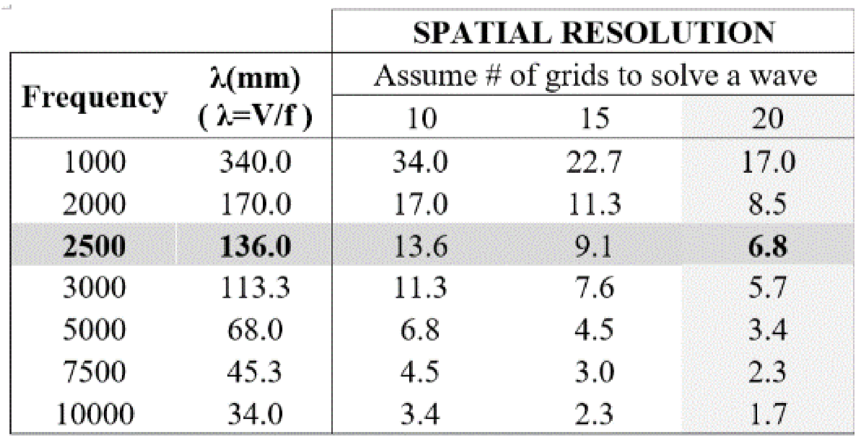

		SPATIAL RESOLUTION		
		Assume # of grids to solve a wave		
Frequency	**λ(mm) (λ=V/f)**	10	15	20
1000	340.0	34.0	22.7	17.0
2000	170.0	17.0	11.3	8.5
2500	**136.0**	13.6	9.1	**6.8**
3000	113.3	11.3	7.6	5.7
5000	68.0	6.8	4.5	3.4
7500	45.3	4.5	3.0	2.3
10000	34.0	3.4	2.3	1.7

Mesh size has both acoustics and aerodynamics limitations. From aeroacoustics perspective, maximum mesh size must not exceed 6.8 millimeters. The model is made to satisfy this limitation by applying maximum mesh size of 5 millimeters. Therefore, model becomes acoustically eligible to predict waves up to 2.5 kHz. Similarly, aerodynamical characteristics of the vehicle should be captured by limiting meshes around the vehicle. This limit is also crucial for convergence of the simulation. Limiter boxes are used to each finite volume element to have a pre-decided maximum size. Figure 13-A and Figure 13-B show examples of such limiter boxes (FLUENT calls them, shape boxes). Vehicle surface mesh is at most 10-15mm depending on location. Also, limiter boxes shown in Figure 13 has a maximum mesh 30-50mm depending on distance between its outer surface and vehicle surface.

Although, unstructured triangular mesh is used, model is meshed using limiter boxes and appropriate acoustic limitations. Figure 14 presents meshes inside and outside of the FW-H surface on the aeroacoustics model. Interior part of the FW-H surface has very dense mesh to capture propagation of acoustic waves from vehicle surface, to all elements on control surface (FW-H surface). Nevertheless, mesh size gradually increases after FW-H surface. This is important for convergence of flow simulation. Total number of mesh in the model is approximately 65 million, which is quite large but it is between practicality limits.

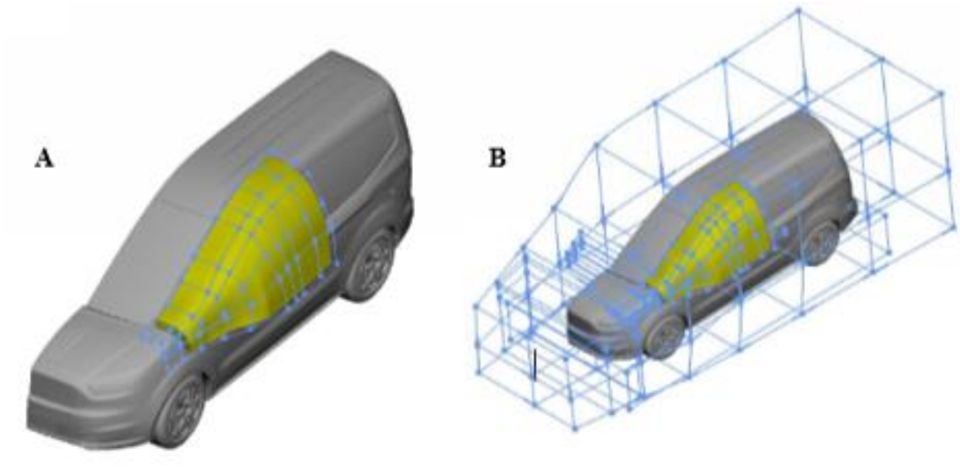

Figure 13: Imaginary boxes to limit maximum mesh sizes

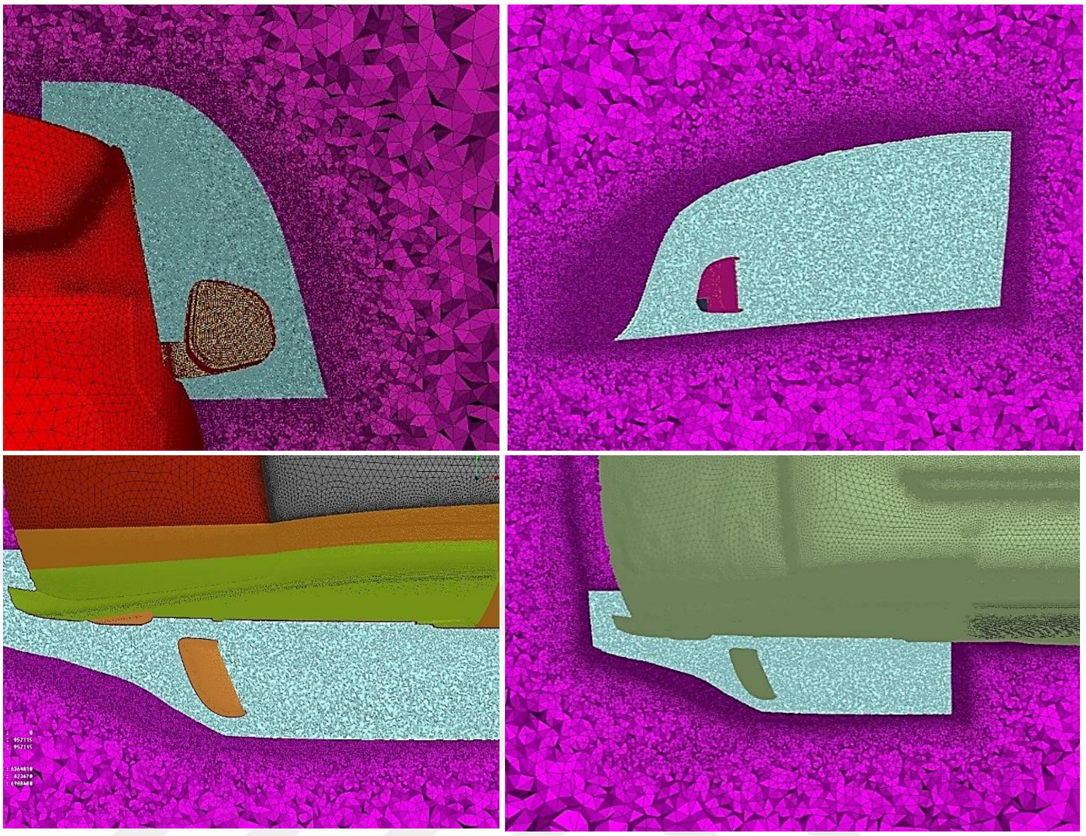

Figure 14: Mesh visuals inside and around the FW-H surface

2.6.2.2. Temporal Resolution

Temporal resolution must be sufficient to achieve a desired maximum frequency. Wagner, et al. [58], Mendonca [59] and others recommend at least 10 time-steps to calculate a sound wave. Therefore, maximum time-step is found as inverse of maximum frequency times number of time-steps. Thus, time-step should not exceed $1/(2500\text{x}10) = 4\text{x}10^{-5}$s.

In his three simulation, Hartmann uses time-steps of transient solution with $\Delta t = 2x10^{-5}$ seconds (sampling frequency of $1/\Delta t = 50000\ Hz$) and transient CFD duration as 0.5 seconds to obtain a converged flow solution [20]. Considering the successful results of this study, the same values are used as beginning points for temporal resolution of this thesis.

However, beginning of transient duration (0.5 seconds) is also momentous. Allowing enough time for vortex-street to develop is remarkable. Considering that the case has high Reynolds number, it is appropriate to refer to Roshko for his study on flows with high Reynolds number [60]. He states that Strouhal number (St) is around 0.25 for a cylinder in a flow with high Reynolds number. Dimensionless Strouhal number describes oscillation of flows. Strouhal number is defined by Vincenc Strouhal [61] as:

$$St = \frac{fL}{U} \tag{43}$$

where f is the frequency of vortex shedding, L is characteristic length and U is flow velocity. Considering the vehicle side mirror and assuming it pretends as a half cylinder with a characteristic length that is around 0.2 m; then, vortex shedding frequency of the vehicle side mirror is found as 45 Hz, which gives a period of 0.022 seconds. Assuming 4 periods of vortex shedding behind the side mirror is sufficient, then 0.1 seconds duration is sufficient to vortex street behind the mirror to develop. Therefore, sampling of transient history should start after a period of 0.1 seconds. Consequently, after 0.1 seconds of non-recorded interval, 0.5 seconds duration should be used for keeping history of flow properties.

However, keeping history of properties on FW-H surface with a time-step of $\Delta t = 2\text{x}10^{-5}$ seconds and total duration of 0.5 seconds makes 25000 time steps. On the other hand, records of cells at each step should be saved. At the end, these should be processed by the FW-H code. A reduction is made such that, transient solution is processed using $\Delta t = 2\text{x}10^{-5}$ seconds time step; but, histories of cells are saved at every 5 time steps (exporting frequency becomes 10 kHz).

In addition, dual time stepping is used. It means that two distinct time steps exist, one is physical (2x10^{-5}s) and the other is pseudo-time which helps convergence of unsteady solution by applying at least 5 sub-iterations at every time step.

2.6.3. Boundary Layer Modelling

In boundary layer model, it is aimed to have low y^+ values, i.e. less than 1. Since low y+ values are obtained, near wall modelling is used. Viscous sub-layers are resolved. First boundary layer height is $0.01\ mm$ with 10 layers forming total height of $2\ mm$. y+ distribution at given conditions and at $t = 0.6\ s$ is visualized as in Figure 15

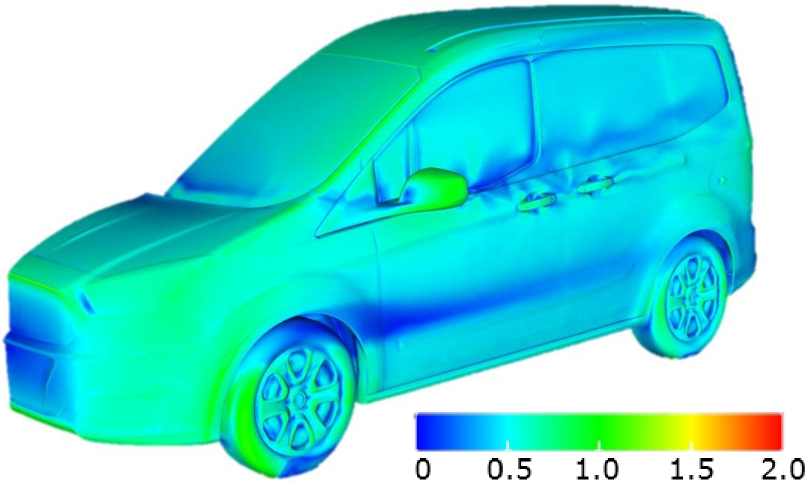

Figure 15: y^+ distribution around the vehicle

Both models, base and aeroacoustics models, use the same CFD simulation methods, as described previously. Boundary layers and mesh parameters are the same (except additional FW-H control surface of aeroacoustics model).

2.7. Far Field Noise Calculation

As mentioned previously, noise calculation is performed by CAA methods. The previous sections of Chapter 2 include details of CFD methodology of CAA. To summarize; CFD is used to resolve the source region, then the FW-H equation calculates the acoustic signal at observer located at a distant location.

For aeroacoustic calculations, porous FW-H surface integral method was introduced in Chapter 1. This section includes a brief introduction for to FW-H equation and its scripted form that is written in FORTRAN language.

The FW-H equation is shown in form of wave equation as follows;

$$\left(\frac{\partial^2}{\partial t^2} - c_o^2 \frac{\partial^2}{\partial x_i \partial x_i}\right)(H(f)\rho') = \underbrace{\frac{\partial^2}{\partial x_i \partial x_i}\left(T_{ij}H(f)\right)}_{\text{Quadrupole}} - \underbrace{\frac{\partial}{\partial x_i}\left(F_i\delta(f)\right)}_{\text{Dipole}} + \underbrace{\frac{\partial}{\partial t}\left(Q\delta(f)\right)}_{\text{Monopole}} \tag{44}$$

Quadrupole, dipole and monopole source terms are governed by,

$$T_{ij} = \rho u_i u_j + P_{ij} - c_0^2 \rho' \delta_{ij} \tag{45}$$

$$F_i = (P_{ij} + \rho u_i(u_j - v_j))\frac{\partial f}{\partial x_j} \tag{46}$$

$$Q = (p_0 v_i + \rho(u_i - v_i))\frac{\partial f}{\partial x_i} \tag{47}$$

Here, time is represented by t and Cartesian coordinates are denoted as x_i, with indices over three dimensions. T_{ij} term stands for Lighthill’s stress tensor, F_i terms represent unsteady force and Q is unsteady mass. These terms form quadrupole, dipole and monopole as shown above. Moreover, ρ and p are total density and total pressure, respectively. f function represents domain outside the surface. Fluid velocities are represented by u_i.

Velocities on surface f are v_i. Speed of sound is c_0. Free stream conditions are represented by subscript 0. Prime notation is used for perturbation terms. Kronecker delta is $\delta_{ij} = 1$ for $i = j$ and it is zero if $i \neq j$. Similarly, Heaviside function is defined as; $H(f) = 1$ for $f > 0$ and $H(f) = 0$ for $f < 0$. Then, Dirac delta function $\delta(f)$ is derivative of the Heaviside function. $\delta(f) = 0$ for $f \neq 0$ but integral of Dirac delta function from a region that includes $f = 0$ leads to a finite value.

Although, the FW-H equation can be solved in time and frequency domains, frequency domain solution is chosen. The main reason is its practicality. Frequency domain solution is faster, compared to solution in time domain. It also gives physical insight into noise mechanisms [62].

Solution to the FW-H equation in frequency domain is defined by Lockard and Casper as in Equation 48 [36]. On the left hand side, $H(f)$ represents the Heaviside function, which indicates that the solution is zero on any point of integration surface.

$$H(f)c_0^2\rho'(y,\omega) = I_T + I_L + I_Q \tag{48}$$

where, the monopole term (also known as “thickness term”) is defined by,

$$I_T = -\int_{f=0} i\omega Q(\xi,\omega)G(y;\xi)ds \tag{49}$$

and the dipole term (also known as “loading term”) is given as,

$$I_L = -\int_{f=0} F_i(\xi,\omega)\frac{\partial G(y;\xi)}{\partial y_i}ds \tag{50}$$

and the volumetric quadrupole term is represented by,

$$I_Q = -\int_{f>0} T_{ij}(\xi,\omega)\frac{\partial^2 G(y;\xi)}{\partial \xi_i \partial \xi_j}d\xi \tag{51}$$

The quadrupole term is small and neglected as a common practice. Considering expense of volumetric calculation, it is advantageous to avoid these terms.

In [63], Lockard simplifies F_i and Q terms of monopole and dipole calculations as in the following forms,

$$F_i = \left(p\delta_{ij} + \rho(u_i - 2U_i)u_j + \rho_0 U_i U_j\right)\hat{n}_j \tag{52}$$

$$Q = (\rho u_i - \rho_0 U_i)\hat{n}_i \tag{53}$$

The term, $\hat{n}$, represents surface normal vectors of a cell. All cell normals are extracted from the model before initiation of simulations.

Contrary to monopole and dipole terms, quadrupole term cannot be reduced. A typical approach is neglecting the volumetric term by locating the FW-H surface around the region where T_{ij} is powerful. Then, it is logical to ignore the quadrupole term.

For a flow in y_1 direction, Lockard [36] gives 3-D Green's function as,

$$G(y;\xi) = \frac{-1}{4\pi d}\exp\left(-ik\left(d - M\left(y_1 - \xi_1\right)\right)/\beta^{*2}\right) \tag{54}$$

with complex number $i = \sqrt{-1}$. Prandtl-Glauert factor is $\beta^* = \sqrt{1 - M^2}$. Mach number is defined as $M = |U_i|/c_0$. Wavenumber term is $k = \omega/c_0$. Also distances between sources and receiver are represented by d, which is expressed as,

$$d = \sqrt{\left(y_1 - \xi_1\right)^2 + \beta^{*2}\left(y_2 - \xi_2\right)^2 + \beta^{*2}\left(y_3 - \xi_3\right)^2} \tag{55}$$

2.7.1. Windowing

In addition, F_i and Q terms are calculated in time domain for all points on the FW-H surface. Fast Fourier Transform (FFT) is used for converting calculated F_i and Q terms into frequency domain. If problem was consisted of periodic data, this could be used directly in FW-H solution. Oppositely, complex flows are not periodic, and hence data is windowed to obtain a periodic input for FW-H code.

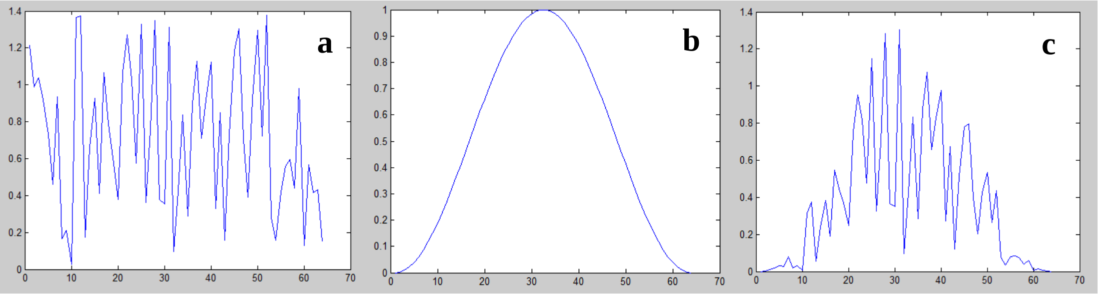

Figure 16: a) Random data, **b)**Hann window and **c)**Windowed data

There are plenty of window functions. Hanning type window, which is widely used, is advantageous because of its good frequency resolution and very low aliasing features. represents a random signal (16.a), hanning window (16.b) and Hann'd data of the random signal (16.c). As seen from this figure, the Hanning window has sine squared shape and touches zero at both ends to eliminate discontinuity. Addition of windowed data consecutively results in a repeated pattern with a periodicity.

2.7.2. High Performance Computing Runs

Analyses consist of time dependent CFD. In order to have fast convergence in transient simulation, a steady state flow solution is beneficial. Respectively, steady state CFD, transient CFD and FW-H calculation form entire sequence of analyses needed by CAA solution. For a detailed car model, these simulations require an intense computational power. High Performance Computing (HPC) system of Ford is used for this purpose. It is possible to use parallel computing on 64 CPUs and 48GB RAM for CFD runs for FLUENT.

2.8. Wind Tunnel Testing

In terms of wind tunnel tests; vehicle stands on four force transducers beneath all four tires. Drag force is calculated from the data obtained by these sensors. Corresponding drag coefficient (C_D) is obtained by,

$$C_D = \frac{2F_{drag}}{\rho U_i^2 A} \tag{56}$$

Since frontal area A, density and velocity of flow are known, C_D is easily calculated. Test is repeated 5 times and mean values are saved as C_D of tested vehicle.

Similarly, aeroacoustics model is tested in the same wind condition with an acoustic array. Unfortunately, test did not include C_D calculation.

The wind tunnel testing is done in Ford Merkenich Wind Tunnel. Wind speed of 130 km/h and 0-degree yaw angle is used. Test is repeated three times. Placement of the vehicle in wind tunnel is shown in Figure 17.

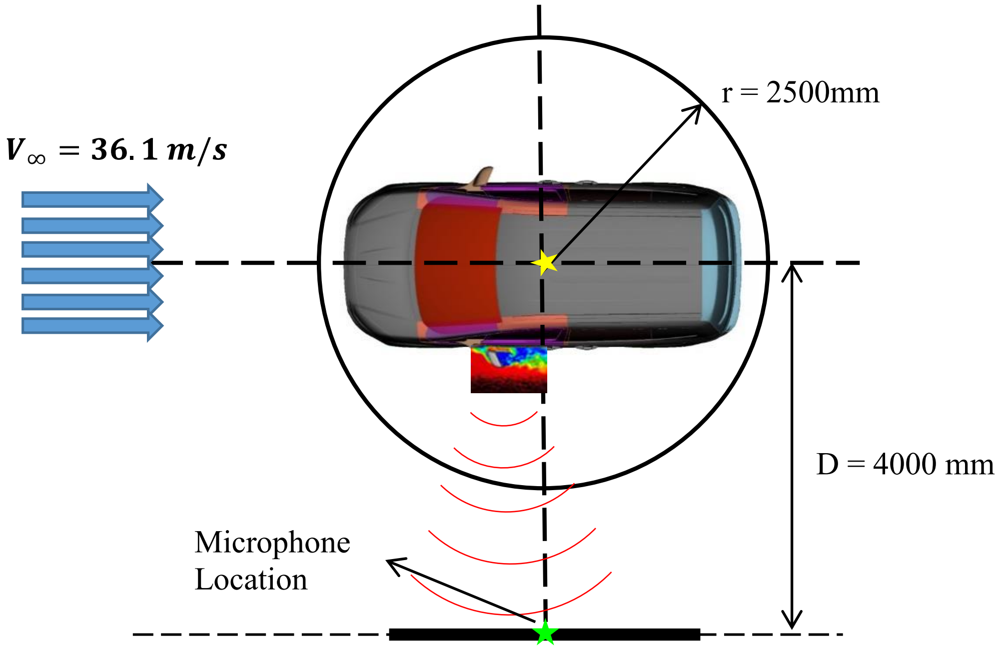

Figure 17: Vehicle and microphone placement of aeroacoustics test

Microphone is located 4 meters away from the car as shown. Instead of using a single microphone, a circular 54 channel acoustic array is used. One of these microphones is reference point for the others. The reference microphone stores time data for acoustic signal, while the rest are used for beamforming algorithm. This algorithm is embedded in Pulse software. Simply, it uses delay of acoustic waves on a number of microphones with known locations for locating the sound sources and their power.

Figure 18: Duct tape by sealing in wind tunnel test

For simplification on CFD modelling, all exterior gaps of the car are sealed using duct tape. Applying this seal makes modelling the car without any gaps possible. Thus, required computational power is decreased. Also, problems due to production tolerances are cancelled by applying tape. In conjunction with gap sealing, rough bumps, rough flanges and the front grille is also sealed. Sealed photos of the car are presented in Figure 18.

CHAPTER 3

RESULTS AND DISCUSSION

In this chapter, aerodynamical and aeroacoustical outcomes of aforementioned method are introduced and discussed. The method can be briefly summarized as a consecutive combination of steady RANS simulation, transient DDES simulation with dual time stepping and acoustical calculation by a FORTRAN code that uses FW-H integral equations.

In order to have reliable numerical results, modelling should be independent of mesh size. Thus, mesh independence is the first study to be shown in this chapter. It is followed by statistical convergence of transient simulation to show that unsteady solution becomes periodic. Then, aerodynamical characteristics of the flow field are presented and discussed, i.e., drag coefficient, pressure coefficient and Q-criterion. Afterwards, aeroacoustics study section is given with a verification test for the FORTRAN code and its prediction of car wind noise. Testing of the code is performed by analytical result of a monopole. After verifying the code, results of wind tunnel testing and FW-H prediction are compared and discussed in detail.

3.1 Study of Numerical Issues

In order to confirm that results of the thesis are credible, mesh independence of simulation model and statistical convergence of numerical calculations are introduced in this section.

3.1.1. Mesh Independence Study

Mesh independence is checked to verify the results are reliable. Different mesh sizes are applied around main aerodynamic noise source region. Comparison is done between a medium mesh size (5 mm) and its refined and coarsened versions. Mesh sizes of 30% finer and 30% coarser meshes are 3.5 mm and 6.5 mm, respectively. These models are simulated and steady state drag coefficients are obtained.

Figure 19 presents comparison of obtained drag coefficients (C_D). As initially selected mesh is refined by 30%, C_D seems changing by 0.42%. Contrarily, 30% coarser mesh results in 5.03% change. Consequently, there is no need for a serious improvement to the initially generated mesh, and no coarsening should be done either.

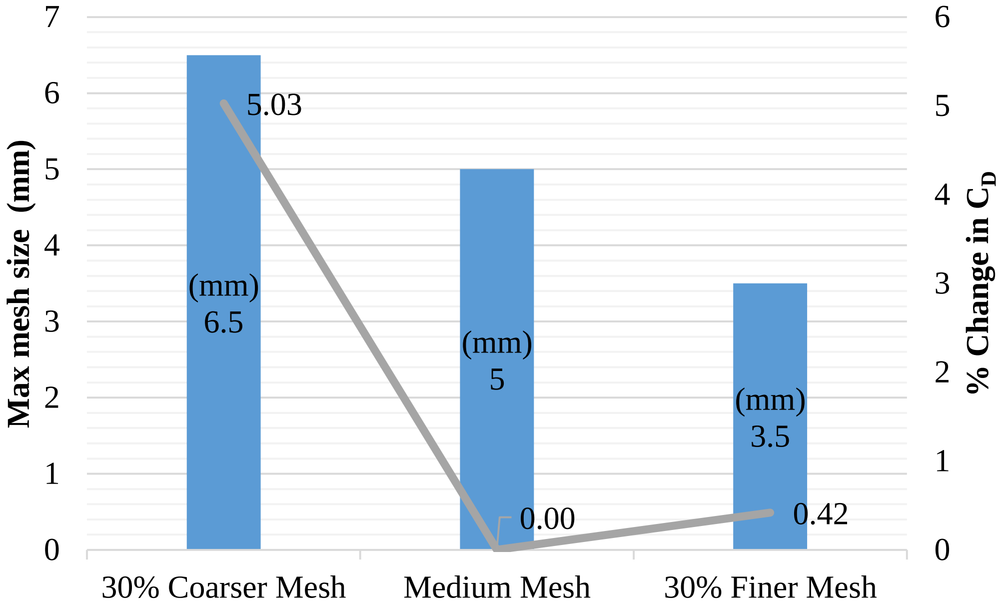

Figure 19: Mesh independence study on aeroacoustics model

Regions causing significant changes are investigated. Equal velocity regions are shown in Figure 20. It seems that, mirror wake notably deviates for coarser meshes.

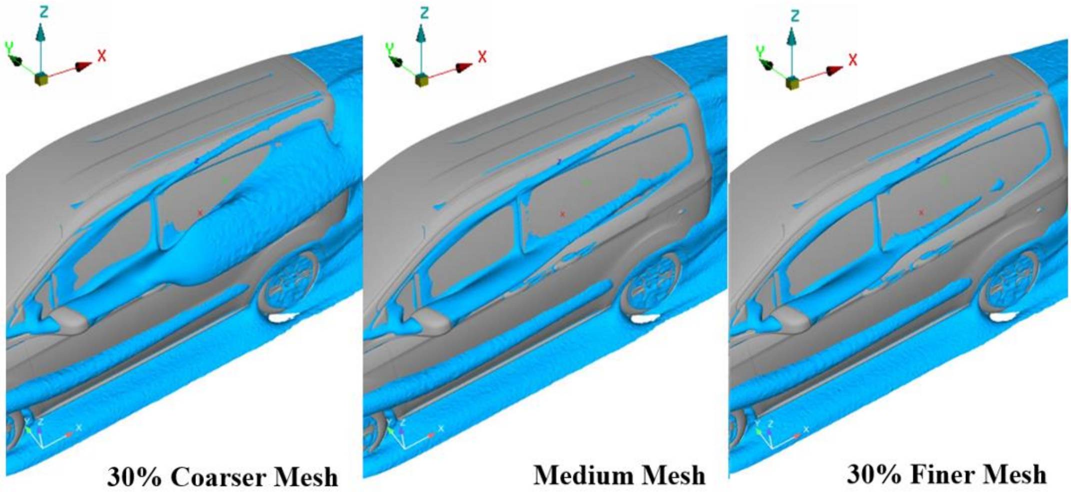

Figure 20: Equal velocity representation on aeroacoustics model

Similarly, velocity distribution in Figure 22 and velocity vector distribution in Figure 22 show considerable changes in mirror wake for coarser mesh. On the other hand, results of finer mesh are barely distinguishable.

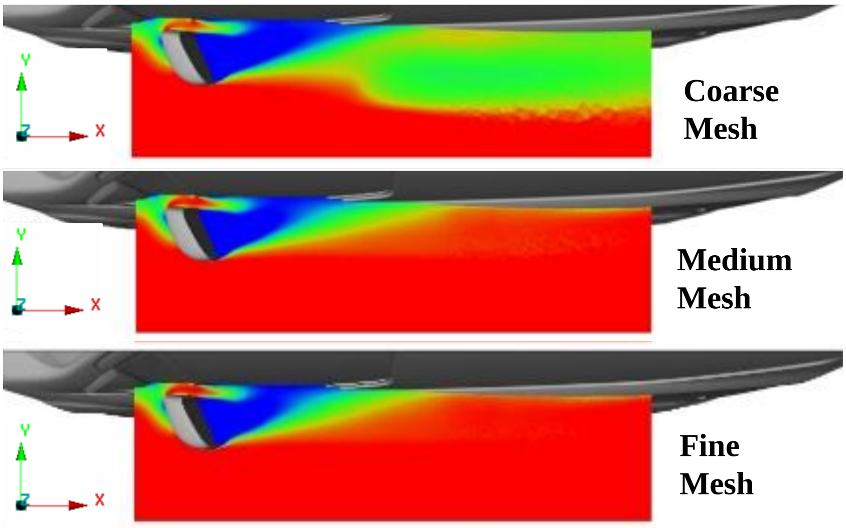

Figure 21: Velocity distribution around aeroacoustics model

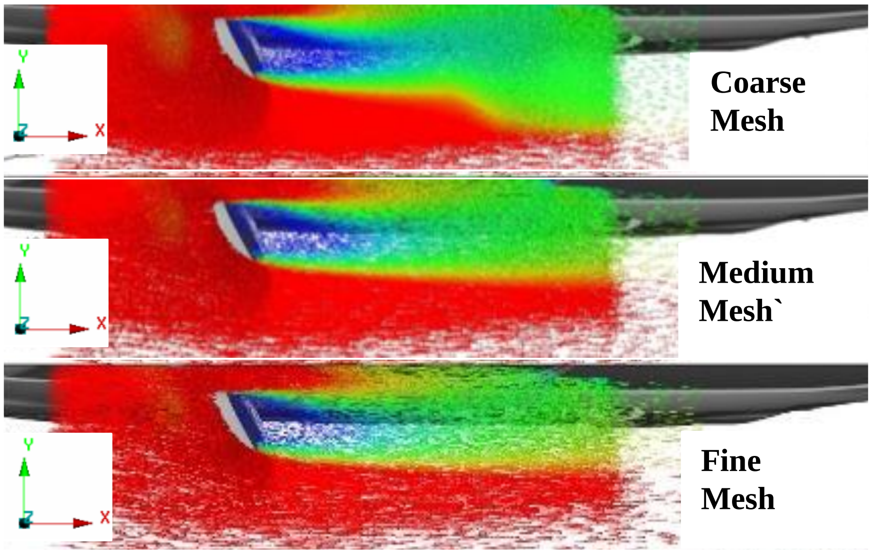

Figure 22: Velocity vector distribution around aeroacoustics model

3.1.2. Statistical Convergence of Numerical Calculations

Statistical convergence of numerical calculations is verified by comparing time averaging of pressure distribution from transient calculations, with pressure values that directly obtained through steady state RANS calculations. Then, statistical convergence is shown by examining residual values of dual-time-stepped transient iterations.

First, 180 points are selected around vehicle side mirror manually. But, the selection is not random. Six vertical and three lateral slices are taken and all slices are represented with 20 grid points.

In total, 180 points are located on the side mirror, as seen in Figure 23. Since flow simulation starts with a steady simulation, steady state pressure values at these points are extracted first. Afterwards, transient simulation is started. Time averaging of pressure data at these points are obtained between $t = 0.1\ seconds$ and $t = 0.6\ seconds$.

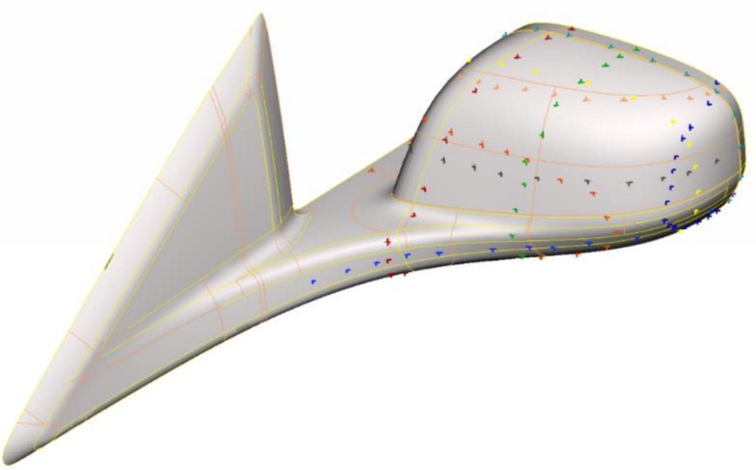

Figure 23: Points around side mirror of aeroacoustics model

The comparison between steady state and time average of transient pressures are shown in Figure 24. The comparison shows that transient calculations got stabilized around meaningful averages, i.e. steady state solution.

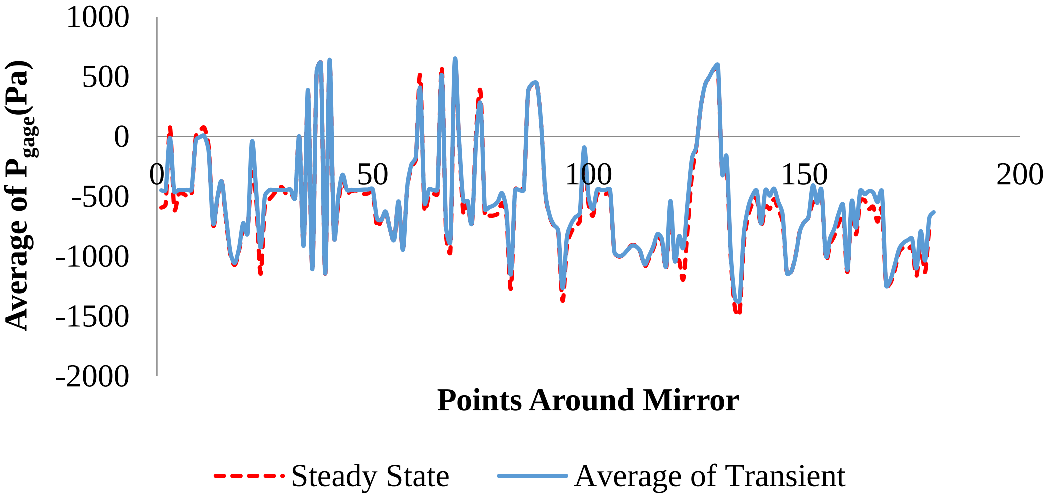

Figure 24: Pressure around side mirror of aeroacoustics model

Secondly, residual values are examined for unsteady solution convergence. The transient solution uses dual time stepping algorithm. It means sub-iterations between two consecutive time steps. These inner iterations are performed to stabilize fluctuations of residuals at each time step.

Continuity and x-velocity (the velocity on axis of flow direction) residuals of transient simulation are normalized and plotted in Figure 25. First plot represents general pattern of corresponding residuals and zoomed graphs are shown on the second and third plots. The zoomed graphs show sub iterations better. Hence, it can be stated that, residuals descend 1 or 2 orders of magnitude, which is an indication of an adequate convergence in transient results.

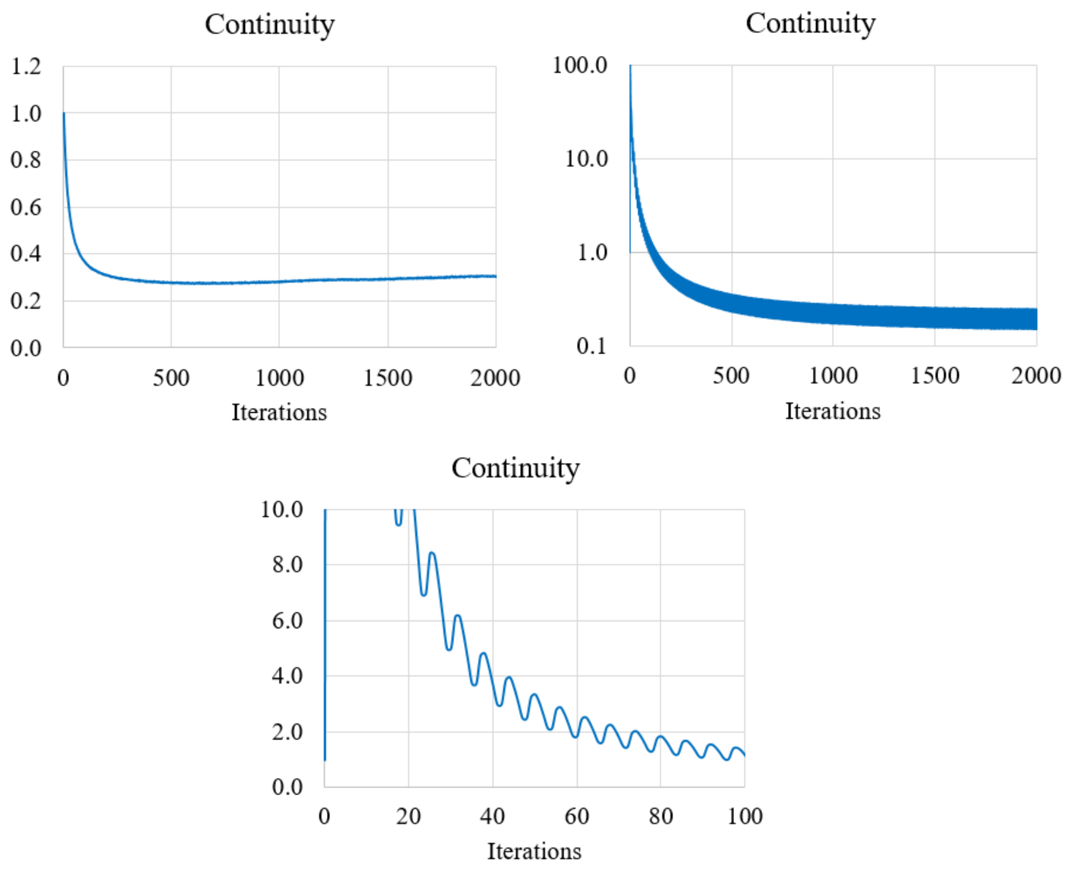
Continuity

Continuity

Continuity

Figure 25: Normalized residuals of aeroacoustics model

3.2 Discussion on Flow Fields

In this section, overall aerodynamical characteristics of aeroacoustics model are verified. At first, drag coefficients of base model, aeroacoustics model and wind tunnel tests are compared. Considering that aeroacoustic wind tunnel test does not include C_D calculation, C_D of aeroacoustics model is compared to C_D of base model. Secondly, C_p distribution of the aeroacoustics model on various cross-sections is compared to corresponding C_p distribution of base model. Finally, flow field around geometry of base model and aeroacoustics model is compared using Q-criterion distribution.

3.2.1. Drag Coefficient

Due to confidential issues, exact values of drag coefficients are not allowed to be shared. Instead, a normalization is used. C_D of wind tunnel test will be given as base and other C_D values will be given as difference between corresponding C_D and wind tunnel test. Therefore, absolute differences between drag coefficients could give useful information.

Table 2: Drag coefficients comparison

	Δ drag coefficients
Wind tunnel test	-
Base model	0.002
Aeroacoustics model	-0.029

Table 2 shows C_D of the three cases. Here, it is obvious that base model gives accurate results compared to the wind tunnel test. The different result of aeroacoustics model can be explained through some modifications that were applied on it. The modifications are iterated one-by-one and their effects on C_D are shown on Table 3.

Table 3: Effects of modifications on drag coefficient of aeroacoustics model

	Item	Effect on C_D
1	**Smooth car bottom**	0.010
2	**Duct taped grille**	0.010
3	**Removed speed lip**	0.008
4	**Duct taped fog lamp**	0.003

First, engine bay and bottom of the vehicle are assumed as completely smooth, because these regions are assumed as not effective as other wind noise sources. Secondly, items 2,3 and 4 are conditions of wind tunnel test and these are reflected on the simulation.

3.2.2. Pressure Coefficient

Next aerodynamical verification is done by comparing pressure coefficients of the base model and the aeroacoustics model on various cross-sections. An example comparison on $y = -0.215\ m$ planes (see Figure 26) will be given in this section.

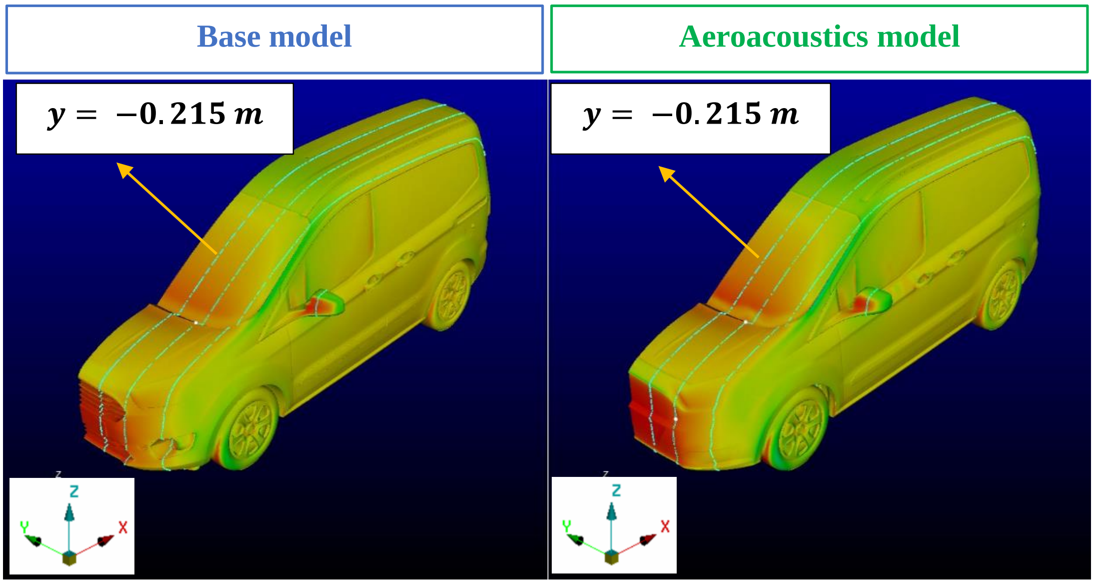

Figure 26: Visuals for cross-sections that are used for C_p comparison

C_p comparison between base and aeroacoustics models on $y = -0.215\ m$ plane is introduced in Figure 27.

It can be seen from Figure 27 that, there are observable deviations on $x = 1.1\ m$ and $x = 1.2\ m$. Corresponding reasons are explained in Figure 28. Namely, these reasons are the disregarded grille openning and speed lip of the aeroacoustics model.

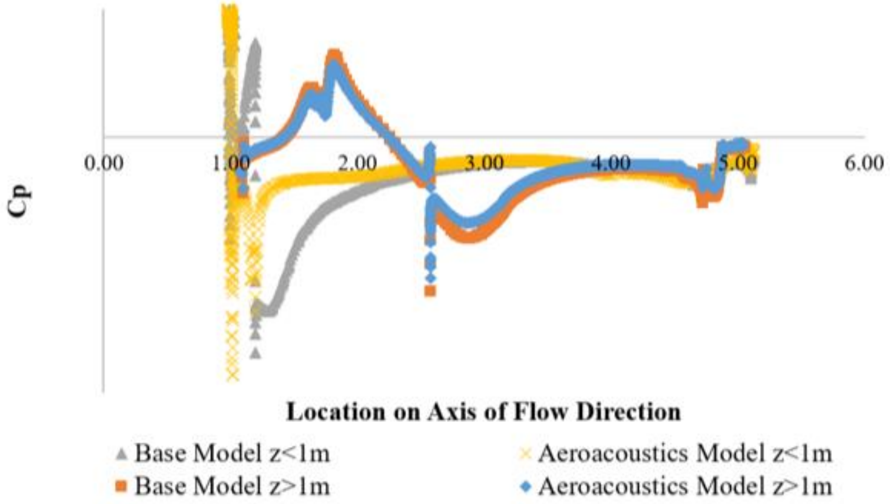

Figure 27: C_p comparison between base and aeroacoustics models

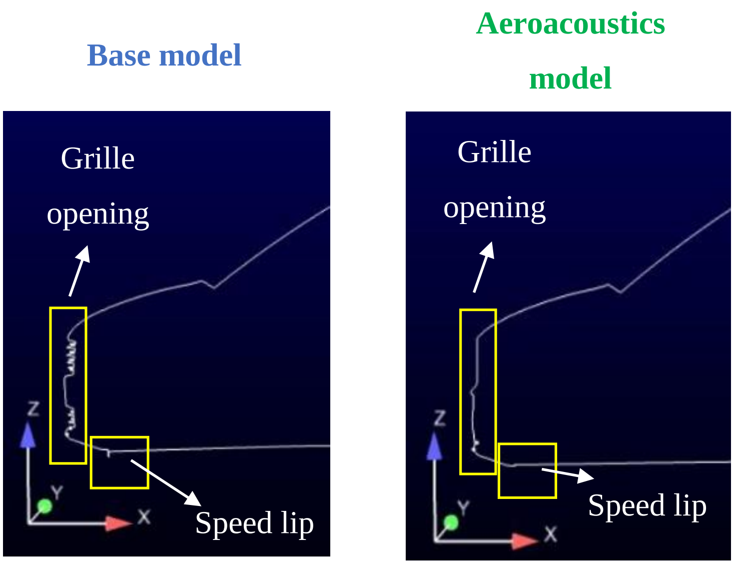

Figure 28: $y = -0.215\ m$ cross-section of base and aeroacoustics models

3.2.3. Q - Criterion

Flow field around vehicle geometry is compared using Q-Criterion, which is defined as local balance between shear strain rate and vorticity magnitude by Holmen [64]. Vortices are defined as regions with greater vorticity magnitude than magnitude of rate-of-strain. Thus, vortex region is defined as positive Q_c region, which is,

$$Q_c = \frac{1}{2}\left(\|\Omega\|^2 - \|S\|^2\right) \tag{57}$$

$$\Omega = \frac{1}{2}\left(\frac{\partial u_i}{\partial x_j} - \frac{\partial u_j}{\partial x_i}\right) \tag{58}$$

$$S_{ij} = \frac{1}{2}\left(\frac{\partial u_i}{\partial x_j} + \frac{\partial u_j}{\partial x_i}\right) \tag{59}$$

Regions with positive Q_c values are plotted in Figure 29 and Figure 30. Three sets of Q_c values, which are $Q_c = 1$, $Q_c = 10$ and $Q_c = 100$, are introduced to validate the aeroacoustics model. These figures consist of visual representation of Q-criterion using side view and top view, respectively. Since the base model is known to be aerodynamically validated, it is used as validation model for the aeroacoustics model.

Equal Q zones of both models are not identical, but general pattern of wake zones of main aerodynamic noise contributor areas are captured well by aeroacoustics model.

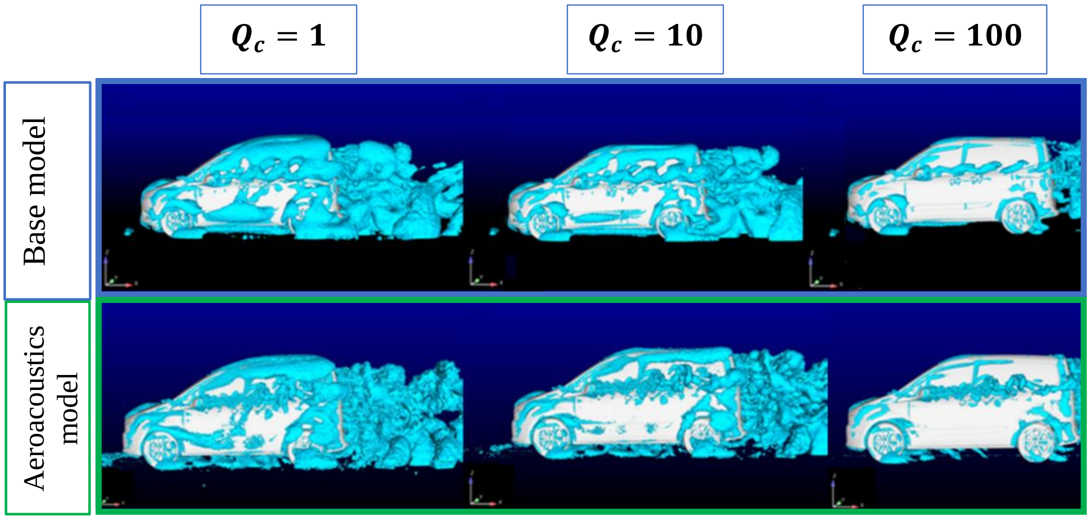

Figure 29: Q-criterion of base and aeroacoustics model side views

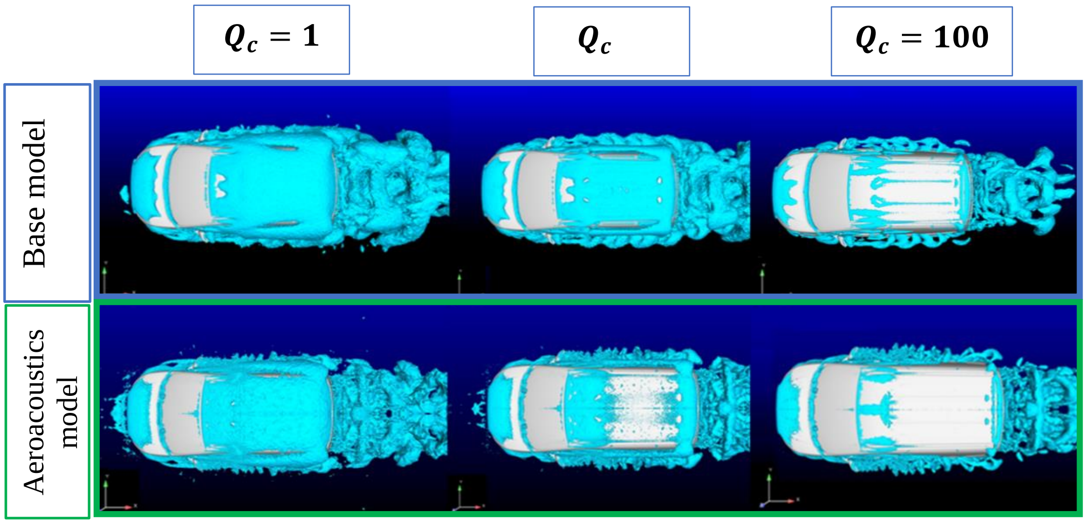

Figure 30: Q-criterion of base and aeroacoustics model top views

3.3 Aeroacoustics Study

Aeroacoustic calculation part of the method uses FW-H integral equations. These equations are embedded in a FORTRAN code. It uses transient flow properties from CFD simulation and calculates far field wind noise at observer location.

This section consists of two main parts. First, the FW-H code is verified through comparing far field results of its prediction and analytical solution of a 3D monopole source. After verification, far field wind noise of the car model is calculated and compared with wind tunnel test result.

Equation 60 introduces analytical solution of the potential function of 3D monopole source, which is defined by Dowling and Ffowcs Williams in [65] ;

$$\phi(x,y,z,t) = -\frac{1}{4\pi d} e^{-ik(d-Mx)/\beta^2+i\omega t} \tag{60}$$

where, d is $\sqrt{x^2+\beta^2 y^2+\beta^2 z^2}$ and ϕ is potential function of the monopole in complex domain. The potential function is used for flow variable calculations. Pressure, velocity and density are calculated by,

$$p = p_0 - \rho\left(\frac{\partial \phi}{\partial t} + U_0 \frac{\partial \phi}{\partial x}\right) \tag{61}$$

$$u = U_0 + \nabla \phi \tag{62}$$

$$\rho = \rho_0 + p'/c_0^2 \tag{63}$$

Furthermore, FW-H equation requires frequency domain values of flow variables. Fourier transform is applied to real parts of variables that are found from above equations. Then, these are used by FW-H equation. Likewise, comparison between analytical solution and FW-H solution will be given in frequency domain, by taking Fourier transform of time domain analytical solution.

As discussed in methodology, a proper FW-H surface should be selected. In this case, it is chosen as a sphere with 1m radius, with its center located on origin (0,0,0) which is also the location of monopole source. Analytical solution is used to obtain flow variables among surface of the sphere for one period. Then, flow variables and geometrical properties on the sphere are used for FW-H calculations.

The monopole source is as a source with angular frequency of $\omega = 4272.5\, rad/s = 680Hz$ and located on (0,0,0). Flow is in x-direction with a uniform freestream Mach number of 0.3. Observer is located at $(5m, 2m, -1m)$.

Time domain analytical solution at observer location is shown in Figure 31,

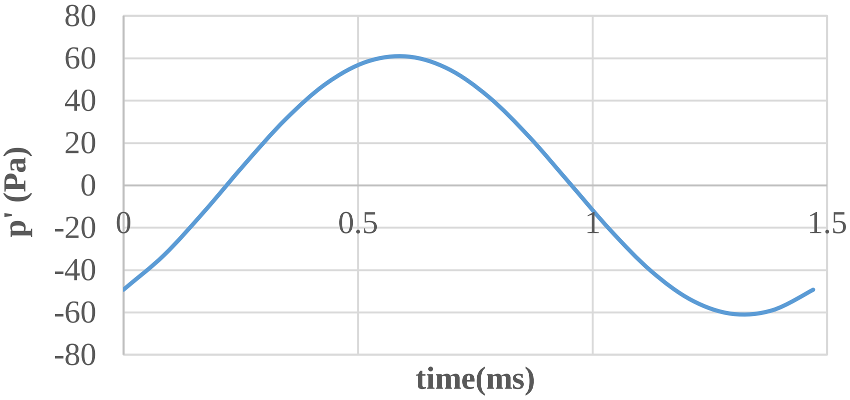

Figure 31: Analytical solution of pressure at observer location

Analytical solution of pressure fluctuations at observer location (Figure 31) is converted from time domain to frequency domain. Figure 32 represents comparison of analytical solution and FW-H solution of pressure fluctuations of a monopole in frequency domain.

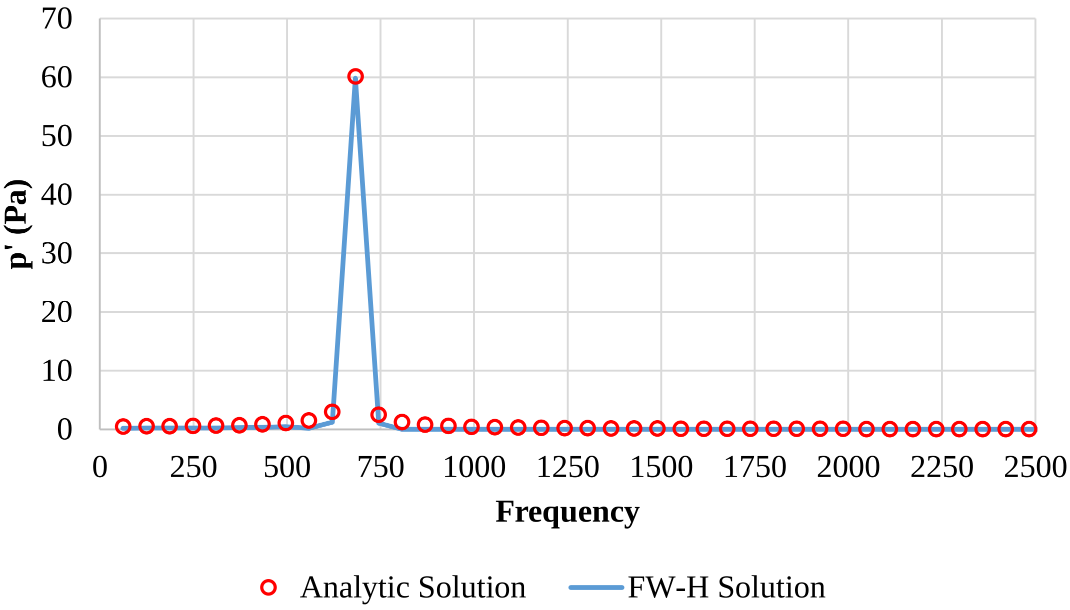

Figure 32: Analytical and FW-H solution of monopole source

It is obvious that Figure 32 can be interpreted as a good correlation between analytical and FW-H solutions. Thus, the FW-H code can be used for real applications.

Wind noise of the vehicle model is calculated using aforementioned FW-H code. History of flow variables, obtained from CFD simulation and geometrical properties of FW-H surface are given as inputs to the code.

Considering the common usage, pressure fluctuations are converted to decibels (dB) at the end of the FW-H code. Test data is also converted into dB unit. The conversion is done using the formula, which is represented as follows;

$$dB = 10 * \log_{10}\left(\frac{Pascals}{P_{ref}}\right)^2 \qquad (64)$$

where, reference pressure is $P_{ref} = 20\ \mu Pa$.

Wind noise is calculated as pressure fluctuations at the microphone position that was used in the wind tunnel test. Arrangement of microphone and car model are visualized in Figure 33. Wind speed is 36.1 m/s in x-direction and yaw angle is set to zero degrees. In addition, as the objectives of the thesis states, frequency interval to be predicted is between 250 Hz and 2500 Hz. This is due to physical limitations that are caused by initial assumptions.

Considering the confidentiality issues regarding Ford Transit Courier vehicle, exact values of far field noise are not given in plots. Instead, length of vertical grid spacings are specified in plots.

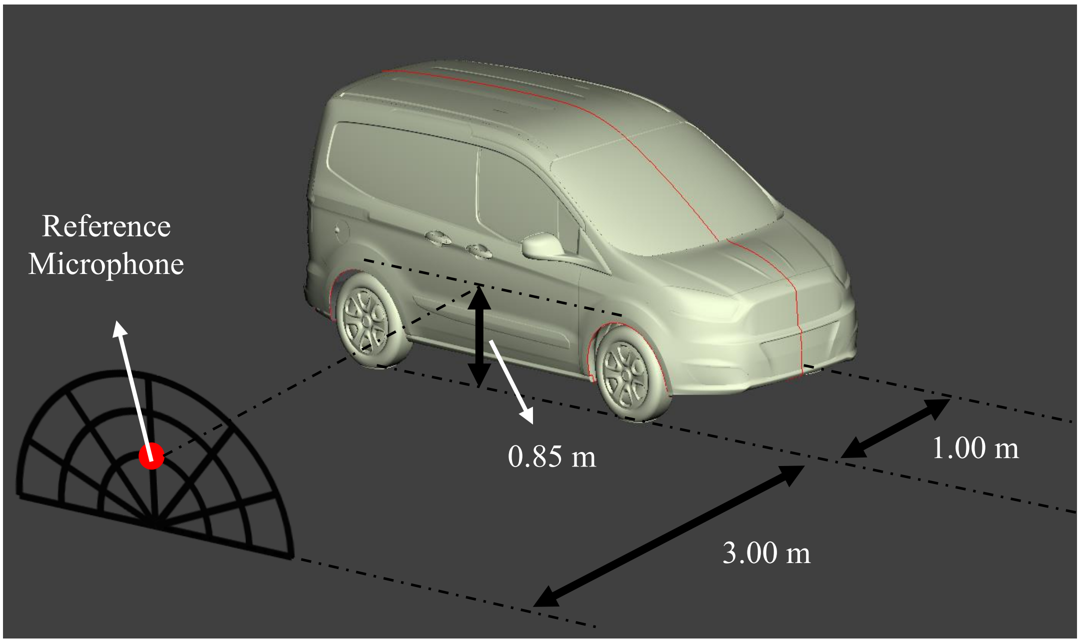

Figure 33: Wind tunnel test setup visualization

Comparison between calculated values and test data is given in Figure 34. It is seen that, calculated data is exceedingly fluctuating. To understand its pattern and general level, moving average is applied to the calculated data only. These are plotted in Figure 35. It should be emphasized that, the test data does not have moving averages.

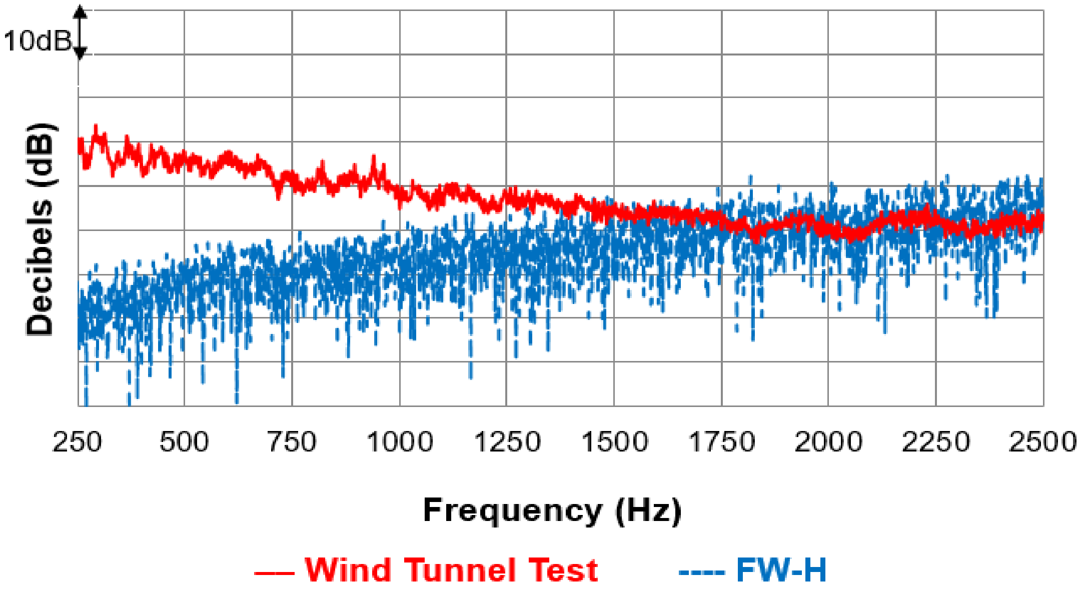

Figure 34: Far field wind noise verification of FW-H method

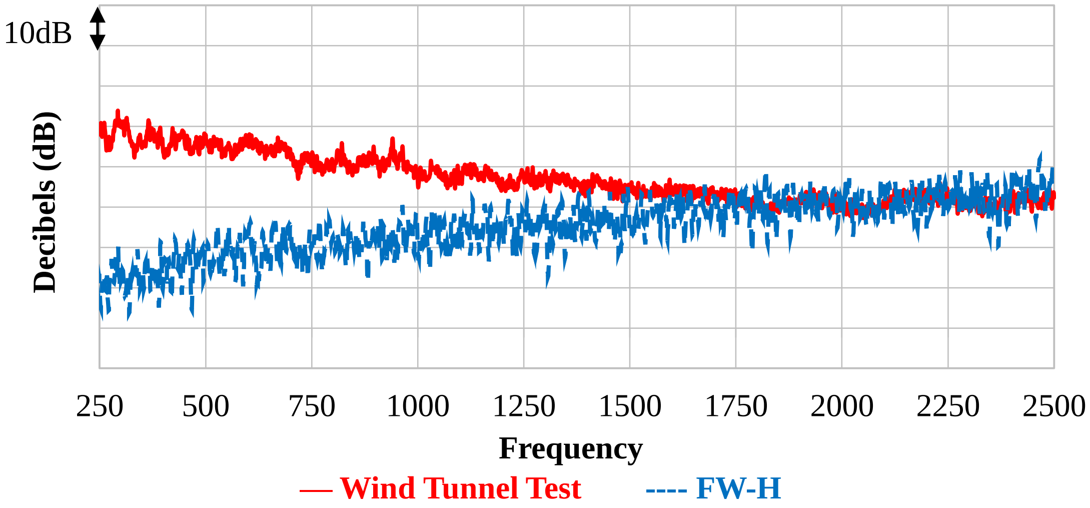

Figure 35: Far field wind noise levels with 6 moving averages on FW-H data

It can be deduced from Figure 35 that test and prediction do not seem to have any relation at lower frequencies. However, values at frequencies that are greater than 1750 Hz seem to be better predicted.

In order to make sure, 1500 Hz - 2500 Hz interval is zoomed in Figure 36. It can be seen from this plot that, level of sinusoidal shape of test data seems to be predicted by FW-H result. On the other hand, even if the FW-H data is plotted using 6 moving averages, excessive fluctuation is still a problem.

Moreover, in order to isolate fluctuations and observe general patterns, using 1/3 or 1/12 octave band representation is a rule of thumb for aeroacoustics applications. Both test data and calculation data are subjected to 1/12 octave band conversion for higher resolution plot compared to 1/3 octave band. Preferred numbers of 1/12 octave band that are specified in British Standard BS2045:1965 are used for center frequencies. The comparison is plotted in Figure 37.

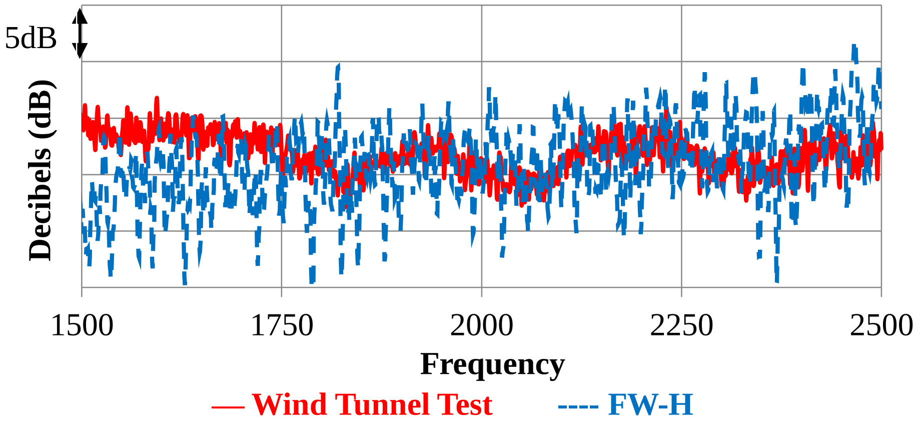

Figure 36: Far field wind noise levels between 1.5 kHz - 2.5 kHz

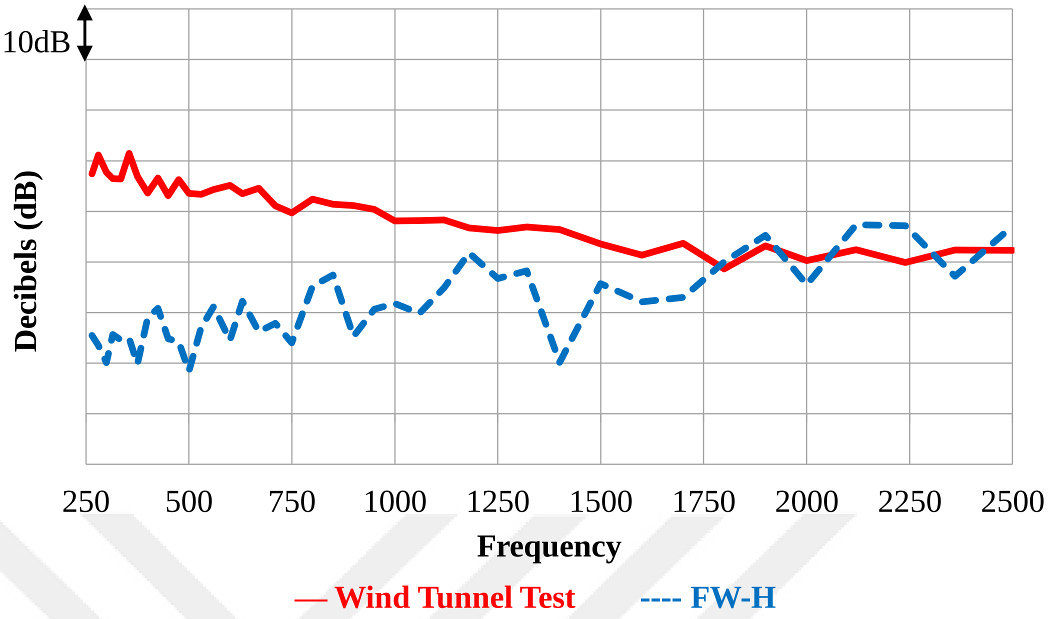

Figure 37: Far field wind noise levels comparison in 1/12 octave band

In 1/12 octave band representation, it is more obvious that, prediction gets better at frequencies higher than 1750 Hz. Still, there are exaggerated predictions due to fluctuations.

Considering the wind tunnel test, which is conducted using a microphone array, acoustic map of the vehicle is available in the software of microphone array. It is used to extract acoustic maps on various frequencies.

Figure 38 shows that effect of side mirror becomes more powerful after some frequency between 1 kHz and 2 kHz. On the contrary, tire cavity is obviously an effective acoustic source that is active in a quite wide frequency interval.

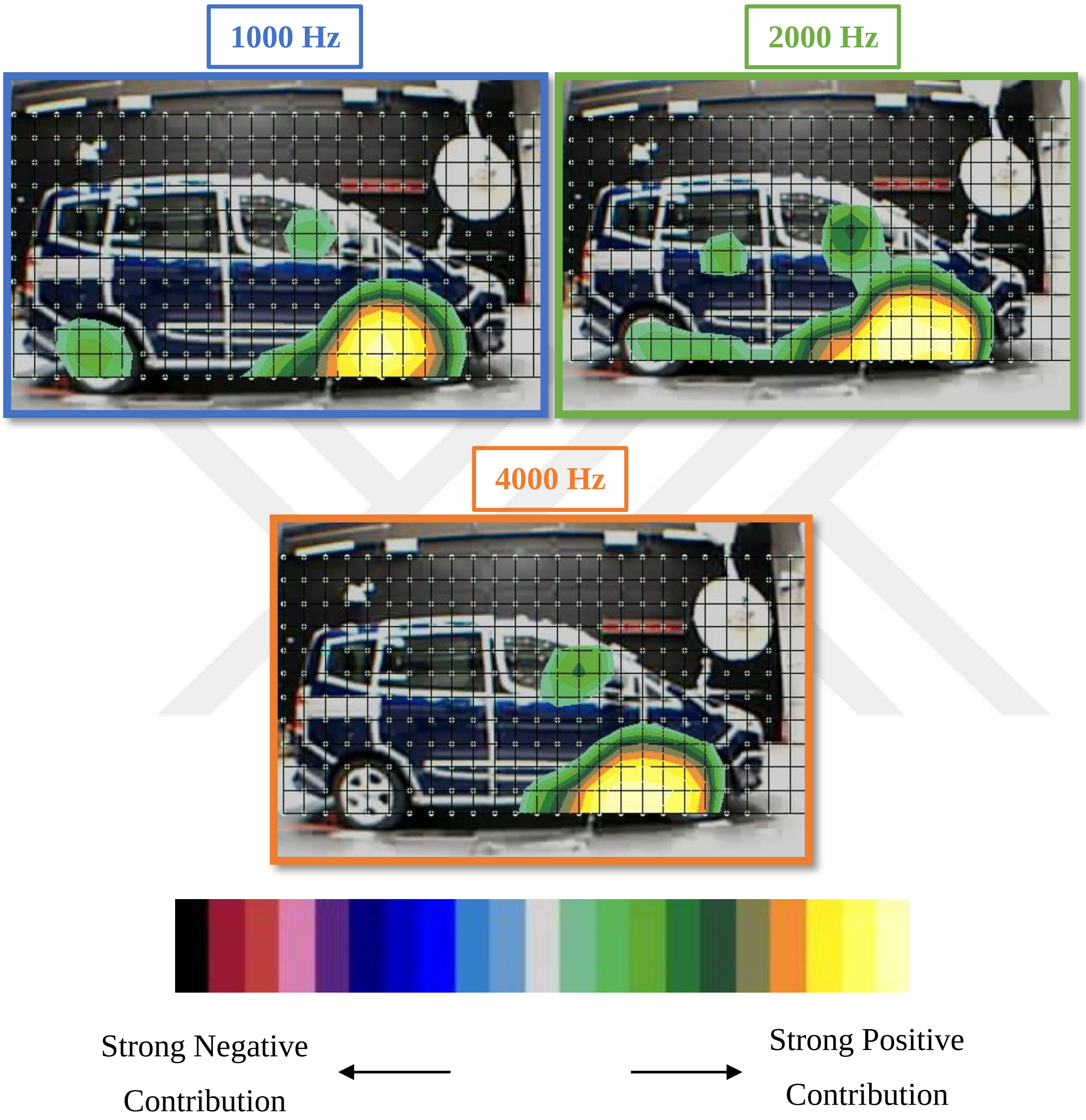

Figure 38: Acoustic map of the vehicle from microphone array data

Figure 38 shows clearly that tire cavity is acoustically dominant in a wide frequency interval. However, acoustic effect of this region is not included in the FW-H surface. The reason is initial assumption that, “aeroacoustically effective sources are located near side mirror”. This assumption is valid in terms of interior noise. On the contrary, it seems, this assumption is not valid for exterior (far field) wind noise. In order to have aeroacoustic contribution of tire cavity, a second FW-H surface should be applied around tire region. On the other hand, attempts to implement a second FW-H surface fail due to flow convergence problems. This may be caused from great number of small elements around noise source regions. A study of Neuhierl, et al. supports the importance of tire zones [24]. They studied an aeroacoustics prediction by closing underflow and tire cavity, test condition and corresponding CFD modelling approach is shown in Figure 39. This approach is also effective for convergence problem. Moreover, this kind of an application significantly relaxes CFD model and its data problem.

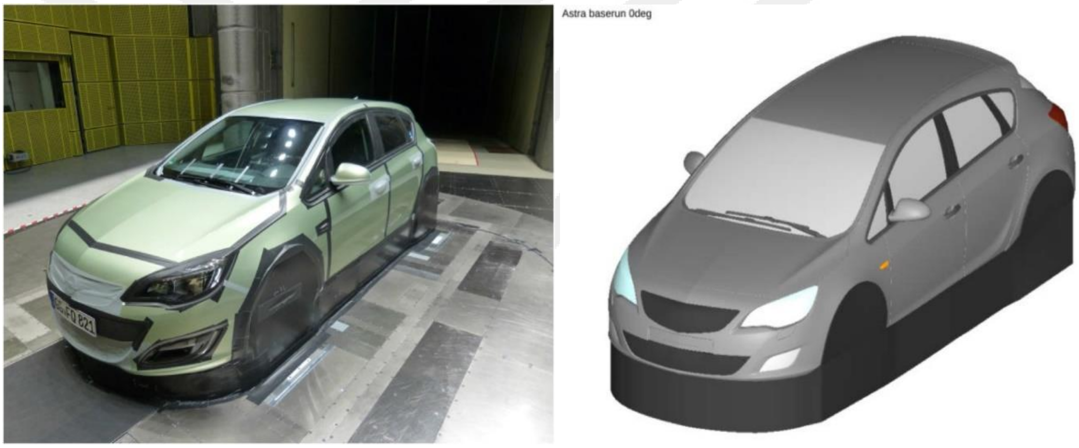

Figure 39: Disregarded tire zones both in test and CFD simulation [24]

It is important to emphasize that a certain frequency interval seems to be predicted, while rest of the frequency band is not. One reason of this situation might be the different patterns on directivity of sound waves that are created by mirror and tire. Since the wind tunnel test and FW-H method are not constructed on a purpose to estimate wind noise directivity, these methods cannot give a feedback about directivity patterns of sound waves.

Supposing the strongest acoustical directivity of mirror is in direction towards the microphone location (sideways, horizontal) and if the sound waves that are created by tire are dominant towards another direction, then the mirror might get powerful around its most effective frequency interval (around 2 kHz). Thus, effect of tire might not be so strong at this frequency range, due to its directivity. Then, difference between test and prediction might be reasonable.

Another supporting possibility of the directivity assumption is position of observer (microphone). Wind noise is recorded by a microphone array, with 54 microphones. But, a useful pressure history is obtainable only from one microphone, which is called as reference microphone, (see Figure 33). This figure effectively represents that the reference microphone is closer to the tires compared to the side mirror for both wind tunnel test and CFD simulation. This might be another explanation of distinct patterns of test and FW-H predictions.

The second possible way to understand non-alignment between test and FW-H prediction method is through Strouhal's equation. Vortex shedding frequency of the side mirror was calculated as 45 Hz in the Section 2.6.2.2. Using a similar approach for a tire with a diameter of 650 mm (a common tire size for these vehicles), the vortex shedding frequency is obtained as 14 Hz (assuming a Strouhal number as 0.25). Side mirror vortex shedding frequency is more than threefold of tire vortex shedding frequency. This might also explain that tire contribution gets much more important at lower frequencies.

CHAPTER 4

CONCLUSION

In this thesis, a real car model's far field wind noise prediction is performed in frequency domain, using Navier-Stokes and Ffowcs Williams & Hawkings equations.

In the beginning, automotive interior noise patterns of the last few years and conforming ways to this trend are introduced. Then, sources of wind noise and other noise types are presented. After identifying target as prediction of wind noise of a vehicle, corresponding solution methods are given in details. Introduction is completed by specifying the objective and the scope of the thesis.

The methodology is determined as a hybrid CAA method, which is a combination of incompressible, DDES turbulence modelled, spatially 3rd order MUSCL discretized, temporally 2nd order implicit discretized, Green-Gauss Node Based gradient evaluated CFD simulation and porous FW-H integral equation calculation for far field.

In the result chapter, aerodynamical and aeroacoustical results of the model are presented. Firstly, study on numerical issues are given. Mesh independence of the model is tested to verify reliability of the results. It is seen that mesh is fine enough, but coarsening the mesh size might result in deviation. Secondly, statistical convergence of numerical calculations is discussed. Unsteady pressure values are shown to be very close to the steady state values. Afterwards, normalized residuals are plotted to show descends of one or two orders of magnitude in dual time stepping of transient simulation. Then, overall aerodynamical values of flow field around geometry are validated, i.e., C_D, C_p and Q-Criterion. In the aeroacoustics study section of this chapter, the FW-H code is verified through a comparison between its prediction and analytical solution of a 3D monopole. It is seen that the code is eligible for such calculations. In the end, far field wind noise of the car model using FW-H integral equations is presented with its wind tunnel test results. Frequency domain solution is converted to 1/12 octave band center frequencies. However, FW-H prediction seems to be aligned with the test results at frequencies higher than 1700 Hz. Possible reasons of deviation are discussed. Yet, a certain cause of this problem could not be addressed. All possible causes indicate importance of tire and tire cavity of the vehicle. Attempts to include this region fail due to convergence issues of CFD simulation.

As a future plan, implementation of tire cavity in FW-H calculations will be completed. It is limited by convergence of CFD simulation, due to more than 100 million meshes in total. But yet, another wind tunnel test is scheduled in 2017 Fall. This test is going to be done in Ford Merkenich Wind Tunnel. In this test, gaps between road and bottom of the vehicle, as well as tire cavity will be closed to disregard underflow (as in [24]). Test will not only be conducted for aeroacoustics calculations, but it will also be conducted for aerodynamical calculations. Therefore, aerodynamical verification of the model will be done much clearly. At the same time, possible variations from results of different models would be altered.

Another fundamental assumption was mentioned in Section 2.6.2.2 that, for reducing outputs of CFD simulation, flow variables were saved at every 5 time steps. This action reduces required free-space and computation need. However, it also results in a lower maximum frequency. Applying interpolation to given data on Table 1 and Table 2, it can be expected that 4 mm mesh size combined with exporting frequency at every **three** time steps would give a maximum frequency around **4 kHz**. This gain is obtained without much difficulty. Thus, CFD exporting frequency will be updated as three time steps, instead of five, and mesh size around main noise contributor regions will be updated by 4 mm, as another next step.

On the other hand, if a goal of completely replacing the aeroacoustic wind tunnel tests with CAA solutions is aimed; then, required maximum frequency to be achieved becomes as 10 kHz (since most automotive aeroacoustic studies are interested in 0.25 kHz – 10 kHz interval). However, this frequency range is beyond practicality limit of this CAA solution, if the same assumptions are applied. Practically, interest of such high frequencies might require alternative solution types to be adapted in real life applications.

REFERENCES

[1] W. Cheng, “Road traffic noise and public health effects,” Northeast Agricultural University, China, 2015.

[2] M. J. Crocker, *Handbook of noise and vibration control*. John Wiley & Sons, Inc., 2007.

[3] “The car interior noise level comparison site,” 2016. [Online]. Available: http://www.auto-decibel-db.com/index_kmh.html. [Accessed: 05-Apr-2017].

[4] Y. Kato, “Numerical simulations of aeroacoustic fields around automobile rear-view mirrors,” *SAE Int. J.*, vol. 1, no. 586, pp. 1–13, 2012.

[5] K. Genuit, “The sound quality of vehicle interior noise: a challenge for the nvh-engineers,” *Int. J. Veh. Noise Vib.*, vol. 1, no. 1/2, pp. 158–168, 2004.

[6] P. Gardonio and S. Elliott, “Active control of structure-borne and airborne sound transmission through double panel,” *J. Aircr.*, vol. 36, no. 6, 1999.

[7] A. E. Duncan, G. Goetchius, and S. Gogate, “Structure borne nvh basics,” in *SAE 2007 NVH Conference*, 2007.

[8] M. A. Burnett, “Aero-acoustic assessment over a vehicle side glass using surface pressure measurements,” *SAE Tech. Pap.*, vol. 26, no. 336, pp. 1–8, 2005.

[9] U. Kim, M. Maunder, P. Grant, and D. Mawdsley, “Developing a car to meet new pass-by noise requirements using simulation and testing,” *SAE Int.*, vol. 1, no. 2319, pp. 1–5, 2015.

[10] G. Zhengqi, W. Yiping, and L. Weiping, “Evaluation of aerodynamic noise generated in a miniature car using numerical simulation,” *SAE Int. J.*, vol. 1, no. 478, pp. 1–10, 2009.

[11] P. Bergamini, M. Casella, and D. F. Vitali, “Computational prediction of vehicle

aerodynamic noise by integration of a cfd technique with lighthill's acoustic analogy," *SAE Int.*, no. 970401, pp. 1–14, 1997.

[12] S. D. Sovani and K. H. Chen, "Aeroacoustics of an automotive a-pillar raingutter: a numerical study with the ffowcs-williams hawkings method," *SAE Int.*, vol. 1, no. 2492, pp. 1–12, 2005.

[13] M. R. Fink, "Airframe noise prediction method," U.S. Department of Transportation, Springfield, Virginia, 1977.

[14] V. Cotoni, D. Blanchet, and P. J. Shorter, "Modeling interior noise due to fluctuating surface pressures from exterior flows," *SAE Int.*, vol. 1, no. 1551, pp. 1–7, 2012.

[15] K. J. Yamamoto, M. J. Donelson, S. C. Huang, and M. C. Joshi, "Airframe noise prediction evaluation," NASA Contractor Report, 1995.

[16] A. Fuchs, E. Nijman, and H. Priebsch, *Automotive nvh technology*. Springer, 2015.

[17] M. J. Lighthill, "On sound generated aerodynamically. I. general theory," in *Proceedings of the Royal Society of London A: Mathematical, Physical and Engineering Sciences*, 1952, vol. 211, no. 1107, pp. 564–587.

[18] D. Russell, J. Titlow, and Y. Bemmen, "Acoustic monopoles, dipoles, and quadrupoles: an experiment revisited," *Am. J. Phys.*, vol. 67, no. 8, 1999.

[19] D. Blanchet, A. Golota, N. Zerbib, and L. Mebarek, "Wind noise source characterization and how it can be used to predict vehicle interior noise," *SAE Tech. Pap.*, vol. 1, no. 2052, pp. 1–16, 2014.

[20] M. Hartmann *et al.*, "Wind noise caused by the a-pillar and the side mirror flow of a generic vehicle model," *AIAA Pap.*, vol. 1, no. 2205, pp. 1–26, 2012.

[21] A. Blanchet, Denis ; Golota, "Wind noise benchmark bmt4," Summary of presentation at KSNVE 2014, 2014.

[22] R. Kotapati, A. Keating, S. Kandasamy, B. Duncan, R. Shock, and H. Chen, "The lattice-boltzmann-vles method for automotive fluid dynamics simulation,

a review," *SAE Tech. Pap.*, vol. 26, no. 57, pp. 1–5, 2009.

[23] S. R. Ahmed, G. Ramm, and G. Faltin, "Some Salient Features Of The Time-Averaged Ground Vehicle Wake," *SAE Tech. Pap.*, no. 840300, pp. 1–34, 1984.

[24] B. Neuhierl, D. Schroeck, S. Senthooran, and P. Moron, "A computational aeroacoustic study of windshield wiper influence on passenger vehicle greenhouse windnoise," *SAE Tech. Pap.*, vol. 1, no. 2051, pp. 1–8, 2014.

[25] F. Farassat and J. Casper, "Towards an airframe noise prediction methodology: Survey of current approaches," *44th AIAA Aerosp. Sci. Meet.*, vol. 5, no. 210, pp. 1–12, 2006.

[26] A. S. Lyrintzis, "Surface integral methods in computational aeroacoustics -from the cfd near-field to the acoustic far-field," *Int. J. aeroacoustics*, vol. 2, no. 2, pp. 1–53, 2003.

[27] Ö. Yalçın, "Development of a high-order navier-stokes solver for aeroacoustic predictions of wind turbine blade sections," Middle East Technical University, 2015.

[28] C. Bogey, C. Bailly, and D. Juvé, "Computation of flow noise using source terms in linearized Euler's equations," *AIAA J.*, vol. 40, no. 2, pp. 235–243, 2002.

[29] B. A. Singer, D. P. Lockard, and G. M. Lilley, "Hybrid Acoustic Predictions," *An Int. J. Comput. Math. with Appl.*, vol. 46, no. 4, pp. 647–669, 2003.

[30] D. P. Lockhard and G. M. Lilley, "The airframe noise reduction challenge," NASA/TM-2004-213013, 2004.

[31] B. A. Singer and Y. Guo, "Development of computational aeroacoustics tools for airframe noise calculations," *Int. J. Comut. Fluid Dyn.*, vol. 18, no. 6, pp. 455–469, 2004.

[32] M. Wang, J. B. Freund, and S. K. Lele, "Computational prediction of flow-generated sound," *Annu. Rev. Fluid Mech.*, vol. 38, pp. 483–512, 2006.

[33] S. Uosukainen, "Foundations of acoustic analogies," *VTT Publ.*, vol. 757, pp.

34–69, 2011.

[34] S. Kumarasamy and K. Karbon, "Aeroacoustics of an automobile a-pillar rain gutter: computational and experimental study," *SAE Tech. Pap.*, vol. 1, no. 1128, p. 12, 1999.

[35] Y. Li, T. Kamioka, T. Nouzawa, T. Nakamura, Y. Okada, and N. Ichikawa, "Evaluation of aerodynamic noise generated in production vehicle using experiment and numerical simulation," *SAE Tech. Pap.*, vol. 1, no. 134, pp. 1–8, 2003.

[36] D. P. Lockard and J. H. Casper, "Permeable surface corrections for Ffowcs Williams and Hawkings integrals," *11th AIAA/CEAS Aeroacoustics Conf.*, vol. 1, no. 2995, pp. 1–13, 2005.

[37] Y. Özyörük and L. N. Long, "A new efficient algorithm for computational aeroacoustics on parallel processors," *J. Comput. Phys.*, vol. 125, pp. 135–149, 1996.

[38] N. Sarigul-Klijn, D. Dietz, D. Karnopp, and J. Dummer, "A computational aeroacoustics method for near and far field vehicle noise predictions," *AIAA Pap.*, vol. 1, no. 513, 2001.

[39] K. S. Brentner and F. Farassat, "An analytical comparison of the acoustic analogy and kirchhoff formulation for moving surfaces," *AIAA J.*, vol. 36, no. 8, pp. 1379–1386, 1998.

[40] A. R. Pilon and A. S. Lyrintzis, "Integral methods for computational aeroacoustics," *AIAA Pap.*, vol. 20, 1997.

[41] A. R. Pilon and A. S. Lyrintzis, "Development of an improved kirchhoff method for jet aeroacoustics," *AIAA J.*, vol. 36, no. 5, pp. 783–790, 1998.

[42] S.-E. Kim, Y. Dai, E. K. Koutsavdis, S. Sovani, N. A. Kadam, and K. M. R. Ravuri, "A versatile implementation of acoustic analogy based noise prediction method in a general-purpose cfd code," *9th AIAA/CEAS*, no. 3202, 2003.

[43] D. Hendriana, S. D. Sovani, and M. K. Schiemann, "On simulating passenger

car side window buffeting," *SAE Tech. Pap.*, vol. 1, no. 1316, p. 12, 2003.

[44] S. Grace, "An overview of computational aeroacoustic techniques applied to cavity noise prediction," *AIAA J.*, no. 510, 2001.

[45] Y. Zhendong, G. Zhengqi, T. Jiyuan, D. Guangping, and W. Yiping, "Numerical analysis and passive control of a car side window buffeting noise based on scale-adaptive simulation," *Appl. Acoust.*, vol. 79, pp. 23–34, 2014.

[46] R. Hayes, A. Fadic, J. Mmbaga, and A. Najafi, "Cfd modelling of the automotive catalytic converter," *Catal. today*, no. 188, pp. 94–105, 2012.

[47] J. Tu, G. Yeoh, and C. Liu, *Computational fluid dynamics: a practical approach*, Second. Australia: Elsevier Ltd., 2012.

[48] C. Kenan and Y. Özyörük, "Detached eddy simulation using a high-order low-dissipation low-dispersion computational meth-od for aeroacoustic purposes," in *8th Ankara International Aerospace Conference*, 2015, pp. 1–11.

[49] L. Davidson, *Fluid mechanics, turbulent flow and turbulence modeling*, 1st ed. Goteborg, Sweden: Chalmers University of Technology, 2011.

[50] I. Khan, "Industrial application of CFD to predict high frequency noise from automotive acoustic devices," The University of Hull, 2014.

[51] P. R. Spalart, "Detached-eddy simulation," *Annu. Rev. Fluid Mech.*, vol. 41, pp. 181–202, 2009.

[52] P. R. Spalart, S. Deck, M. L. Shur, K. D. Squires, M. K. Strelets, and A. Travin, "A new version of detached-eddy simulation, resistant to ambiguous grid densities," *Theor. Comput. Fluid Dyn.*, no. 20, pp. 181–195, 2006.

[53] I. Fluent, "Fluent 6.3 user's guide," 2006.

[54] T. Shih, W. Liou, A. Shabbir, Z. Yang, and J. Zhu, "A new k-epsilon eddy viscosity model for high reynolds number turbulent flows: model development and validation," Cleveland, Ohio, 1994.

[55] J. Her and W. B. Coney, "Wind noise challenge in the automobile industry," *J. Acoust. Soc. Am.*, vol. 103, no. 5, pp. 2850–2851, 1998.

[56] R. Powell *et al.*, “Simulation of Underbody Contribution of Wind Noise in a Passenger Automobile,” *SAE Int. J. Passeng. Cars - Mech. Syst.*, vol. 6, no. 2, pp. 1251–1261, 2013.

[57] D. Wilson, N. Symons, E. Patton, and P. Sullivan, “Simulation of sound propagation through high-resolution atmospheric boundary layer turbulence fields,” in *16th Symposium on Boundary Layers and Turbulence*, 2004.

[58] C. Wagner, T. Hüttl, and P. Sagaut, *Large-eddy simulation for acoustics*, 1st ed. Cambridge University Press, 2006.

[59] F. Mendonca, A. Read, S. Caro, and K. Debatin, “Aeroacoustic simulation of double diaphragm orifices in an aircraft climate control system,” *11th AIAA/CEAS*, no. 2976, 2005.

[60] A. Roshko, “Experiments on the flow past a circular cylinder at very high Reynolds number,” *J. Fluid Mech.*, pp. 345–356, 1961.

[61] V. Strouhal, “Über eine besondere art der tonerregung,” *Ann. Phys.*, 1878.

[62] E. Gutmark, B. Callender, and S. Martens, “Aeroacoustics of turbulent jets: flow structure, noise sources, and control,” *JSME Int. J.*, vol. 49, no. 4, pp. 1078–1085, 2006.

[63] D. P. Lockard, “An efficient, two-dimensional implementation of ffowcs williams and hawkings equation,” *J. Sound Vib.*, vol. 229, no. 4, pp. 897–911, 2000.

[64] V. Holmén, “Methods for vortex identification,” Lund University, 2012.

[65] A. Dowling and F. Williams, *Sound and sources of sound*. Chichester, Horwood, 1983.